Novel copper-drugs bearing dipodal *bis*-mercaptobenzimidazoles: Synthesis, crystal structures, *in vitro* biological activities, DNA binding, DFT calculations and molecular docking

Maryam Kia [a], Mitra Ghassemzadeh [a,*], Mahboube Eslami Moghadam [a], Maryam Saeidifar [b], Farshid Mohsenzadeh [a], Olaf Fuhr [c], Dieter Fenske [c]

[a] *Department of Inorganic Chemistry, Chemistry & Chemical Engineering Research Center of Iran, Pajoohesh Blvd., 17th Km of Tehran–Karaj Highway, Tehran 14968-13151, Iran*
[b] *Department of Nanotechnology and Advanced Materials, Materials and Energy Research Center, Karaj, Iran*
[c] *Institut für Nanotechnologie and Karlsruhe Nano Micro Facility (KNMFi), Karlsruher Institut für Technologie, Kaiserstraße 12, 76131 Karlsruhe, Germany*

Keywords:
Dipodal 2-mercaptobenzimidazole ligands
Copper(II) complexes
Anticancer and antibacterial activities
DNA interaction
Molecular docking

A B S T R A C T

Three novel copper(II) complexes, **1**–**3**, bearing dipodal *bis*-mercaptobenzimidazole derivatives based on *ortho*-, *meta*- or *para*-xylene (**L1**, **L2**, and **L3**) were successfully prepared and characterized by using various spectral techniques, including elemental analysis, FT-IR, ^{1}H NMR, and UV–Vis spectroscopy, LC-MS spectrometry and TGA. The analysis revealed that the ligand/metal molar ratio in all copper(II) complexes is 1:1 and the ligand coordinates as a neutral N-donor onto metal center. Additionally, the crystal structures of **L1**, **L2**, **L3**, and copper (II) complex **2** were determined using single crystal X-ray diffraction (SC-XRD) analysis. Copper(II) complexes **1**–**3** displayed significant stability at pH range of 4–10. The antibacterial effect of ligands and complexes was tested against both gram-negative (*Escherichia coli, E. coli ATCC 25922 PTCC 1399*) and gram-positive (*Staphylococcus aureus, S. aureus ATCC 6538 PTCC 1112*) bacterial strains. It should be noted that the complexes showed enhanced antibacterial activity (up to 99 %) when compared to their free ligands. The *in vitro* studies of all synthesized compounds consisted of testing them against the human colorectal carcinoma cancer cell line (*HCT-116*) using the MTT assay. The findings revealed that the copper(II) complexes exhibited lower CC_{50} values (CC_{50} ranging from 0.045 mM to 0.135 mM) compared to their corresponding ligands (CC_{50} ranging from 0.150 mM to 0.240 mM) and carboplatin (CC_{50} 0.165 mM), indicating higher anticancer activity of the complexes. Additionally, DAPI staining and fluorescence spectroscopy (at three different temperatures) were performed to further examine the impact of complexes **1**–**3** on inducing apoptosis and to explore their interaction with DNA, respectively. The results revealed a dynamic quenching mechanism, with hydrophobic forces playing a dominant role in the binding process. The viscosity measurements indicated that all complexes could interact in a groove binding manner with DNA. Density functional theory (DFT) calculations were employed to support the structural and vibrational studies and to predict the chemical reactivity. Docking simulations were conducted to evaluate their behavior of the synthesized compounds towards DNA (PDB: 1BNA). These results suggested that various elements, including NH groups, imidazole rings, thioetheric sulfur atom and sulfate moieties of ligands and complexes, are involved in groove binding with DNA.

1. Introduction

According to reports from The World Health Organization, cancer stands as the second most prevalent cause of mortality in human societies, following stroke and cardiovascular diseases [1]. The advent of platinum-based complexes, including *cis*-platin in 1965, carboplatin in 1989, and oxaliplatin in 1996 [2,3], marked a significant development in the field of anticancer drugs. The successful application of these metal-based complexes, also known as “metallo-drugs” has intrigued chemists, sparking widespread research in the field of medicinal inorganic chemistry [4–8]. Despite the proven therapeutic effectiveness of platinum drugs against various cancer cell lines, their use is restricted by

* Corresponding author.
E-mail address: mghassemzadeh@ccerci.ac.ir (M. Ghassemzadeh).

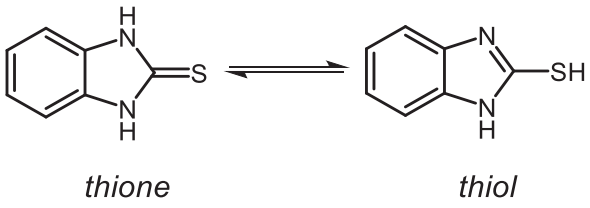

Scheme 1. Tautomerism in 2-mercaptobenzimidazole.

issues such as low solubility, drug resistance, and severe side effects [9,10]. Consequently, researchers face a substantial challenge in the pursuit of alternative drugs to effectively treat different forms of cancer with minimal adverse effects.

To date, numerous metal coordination complexes have been formulated and approved for use as diagnostic and therapeutic agents [10–20]. Notably, copper drugs have gained an increased attention due to copper's essential role as an endogenous metal element involved in various biological processes [21–23]. In contrast to platinum complexes, which establish covalent binding with DNA, copper complexes employ non-covalent interactions, such as intercalation, electrostatic attraction, and groove binding, broadening their spectrum of biological activities [24]. Several copper complexes have been reported to demonstrate enhanced efficacy and lower toxicity compared to conventional platinum-based complexes. These complexes have demonstrated a range of biological activities, including anti-cancer [24–28], anti-viral [29–31], anti-inflammatory [32,33], and antimicrobial activities [34,35].

Biological efficacy and stability are central themes in current cancer research. Therefore, it is crucial for new metallo-drug alternatives to demonstrate both thermodynamic and kinetic stability. In this regard, the utilization of bulky ligands with chelating sites comprising donor atoms (N, O, S) is strongly recommended [36–38]. The recommendation is based on the fact that the bioactivity of these ligands and complexes arises mainly from the presence of an azomethine group (>N═CH—) and the N—C═S moiety [39,40]. Additionally, the presence of heteroatoms (nitrogen, sulphur and oxygen) increases the ability of complex to form hydrogen bonds with nucleic acids facilitating the interaction with DNA [41]. On the other hand, previous research has demonstrated that the presence of aromatic heterocycles in metallo-drugs may affect their biological properties in two ways: (i) these ligands increase the lipophilicity of the complex, thereby facilitating its movement through phospholipid bilayer membranes, and (ii) they strengthen the interaction between DNA and the aromatic rings of the metal complex through π–π interactions [22]. Hence, the choice of a suitable ligand with these properties is of paramount importance.

2-mercaptobenzimidazole derivatives, as representatives of thione-substituted benzene-fused imidazoles, have drawn considerable attention in various fields of science [42–44]. These diazaheterocyclic motifs, found in various biomolecules like albendazole, mebendazole, vitamin B_{12} and thiabendazole [45–47], play a significant role in medicinal chemistry. They are known to display diverse biological activities such as antibacterial, antimicrobial, analgesic, antihistamine, anticonvulsant, antioxidant, and anti-inflammatory activities [48–50].

From a chemistry point of view, these compounds have two distinctive characteristics: (i) the presence of both hard and soft donor atoms (nitrogen and sulfur, respectively), and (ii) thione–thiol tautomerism (Scheme 1). The former allows these ligands to coordinate to various main-group and transition-metal ions, while the latter provides them with the ability to act as either a neutral or deprotonated anionic ligand, leading to the formation of fascinating molecular structures. In this context, a number of metal complexes based on 2-mercaptobenzimidazole derivatives adopting various coordination modes have been reported, namely S-donor ligand (η^1-S or μ_2-S mode) [51–54], N-donor ligand [55], η^2-N,S chelating ligand [56–58] and N,S bridging ligand [59].

Taking into account the potential of 2-mercaptobenzimidazole for biological applications and our ongoing interest in the chemistry of aromatic N,S-heterocycles and their transition-metal coordination complexes [60–65], we hereby present the synthesis and characterization of three *bis*-2-mercaptobenzimidazole compounds, **L1**–**L3**, and their corresponding copper(II) complexes **1**–**3**. In order to establish the coordination mode of **L1**–**L3** in complexes **1**–**3**, we attempted to determine the molecular structures of free ligands and their complexes by the SC-XRD technique. To evaluate their biological properties, the antibacterial activity of all synthesized compounds against two bacterial strains (*E.coli* and *S.aureus*) was first studied. Additionally, their potential antitumor effects were evaluated through MTT assay and their ability to induce apoptosis was examined using AO/PI staining on the human colorectal cell line (*HCT-116*). Besides, the interaction between complexes **1**–**3** and DNA, which is a primary target for new therapeutic agents [66,67] was investigated using fluorescence spectroscopy. Furthermore, viscosity measurements, density functional theory (DFT) calculations and docking experiments were performed to rationalize the experimental data and to gain a better insight into the interaction of the synthesized compounds and DNA.

2. Experimental section

2.1. Materials and instruments

All reagents and solvents were purchased from Merck and Sigma-Aldrich and used without further purification. 2-Mercaptobenzimidazole (98 %), 1,2-*bis*(chloromethyl)benzene (98 %), 1,3-*bis*(chloromethyl)benzene (98 %), 1,4-*bis*(chloromethyl)benzene (98 %), copper (II) sulfate pentahydrate (98 %), potassium hydroxide (KOH, 85 %), dimethylformamide (DMF, 99.5 %), ethanol (99.2 %), methanol (MeOH, 99.9 %), dimethylsulfoxide (DMSO, 99.8 %), ethyl acetate (95.5 %) and *n*-hexane (95 %), and CertiPUR® buffer solutions (pH 4, 7, and 9). Compounds **L1**–**L3** were prepared according to the slightly modified procedure [68]. Calf thymus DNA (DNA), ethidium bromide (EB), and phosphate buffered saline tablets (PBS) were purchased from Sigma–Aldrich. The human colorectal carcinoma cancer cell line, (*HCT-116*), was obtained from the cell bank of the Pasteur Institute in Tehran (Iran). The microorganisms used in this study were obtained from the microorganism bank of the Iranian Biological Resource Center. The FT-IR spectra were recorded on a PerkinElmer 883 spectrometer (KBr pellets 4000–400 cm ^{1}). Melting points were recorded on a Büchi B545 melting point apparatus and are uncorrected. ^{1}H NMR spectra were acquired on a Bruker-AQS AVANCE instrument (500 MHz), and the ^{1}H chemical shift values are reported in parts per million (ppm) relative to the internal standard TMS ($\delta = 0$ ppm). The UV–Vis absorption spectra were recorded with a Leaman inductively coupled plasma spectrometer in the range of 200–1100 nm. Thermogravimetric analysis (TGA) was performed on a Mettler-Toledo TGA/SDTA 851e thermal analyzer in a flowing air atmosphere at a heating rate of 10 °C per min from 25 to 900 °C. The chemical composition was determined using energy-dispersive X-ray spectroscopy (EDX, Oxford Instruments, Oxford, UK). The powder X-ray diffraction (P-XRD) measurements were performed using an X'PERT-PRO diffractometer equipped with a Cu anode that generated Cu K_α radiation ($\lambda = 1.5406$ Å). The fluorescence measurements were performed using a Hitachi fluorescence spectrophotometer (MPF-4 model) equipped with a thermostat bath and a 1.0 cm quartz cell.

Viscosity measurements were performed by an Ostwald microviscometer (SCHOT-geräte, Germany) at room temperature. The UV–Vis absorption spectra at various pH levels were recorded on a Agilent 8453 spectrophotometer. The values of absorbance of aqueous DMSO solution of complexes **1**–**3** (1×10^{3} M) were measured at various pH levels using a pH meter (calibrated with the standard CertiPUR® buffer solutions, pH 4, 7, and 9) under ambient conditions.

Table 1
Crystallographic data for **L1**, **L2**, **L3** and complex **2.**

	L1	L2	L3	Complex 2
Empirical formula	$C_{22}H_{18}N_4S_2$	$C_{22}H_{18}N_4S_2$	$C_{22}H_{18}N_4S_2$	$C_{50}H_{50}Cu_2N_{10}O_{10}S_6$
Formula weight	402.52	402.52	402.52	1270.44
Temperature/K	180	180	180	180
Crystal system	orthorhombic	monoclinic	monoclinic	monoclinic
Space group	*Pbcn*	*C2/c*	$P2_1/c$	$P2_1/n$
a/Å	24.1292(12)	25.8267(9)	10.8065(11)	12.3510(13)
b/Å	8.5744(5)	9.6369(2)	9.3671(6)	18.0563(13)
c/Å	9.8098(4)	9.7617(3)	10.1895(9)	12.8554(11)
α/°	90	90	90	90
β/°	90	93.925(3)	107.304(7)	106.057(7)
γ/°	90	90	90	90
Volume/Å^3	2029.58(18)	2423.88(12)	984.75(15)	2755.1(4)
Z	4	4	2	2
ρ_{calc}g/cm^3	1.317	1.103	1.358	1.531
μ/mm ^{1}	0.277	1.354	0.286	3.634
F(000)	840.0	840.0	420.0	1308.0
Crystal size/mm^3	0.16 × 0.12 × 0.1	0.18 × 0.16 × 0.03	0.15 × 0.07 × 0.06	0.04 × 0.035 × 0.03
Radiation	MoKα (λ = 0.71073)	GaK$_\alpha$ (λ = 1.34143)	MoK$_\alpha$ (λ = 0.71073)	CuK$_\alpha$ (λ = 1.54186)
2Θ range for data collection/°	3.376 to 65.106	8.522 to 124.994	3.948 to 55.994	12.142 to 135.946
Index ranges	$35 \le h \le 36$ $12 \le k \le 12$ $9 \le l \le 14$	$33 \le h \le 34$ $12 \le k \le 12$ $12 \le l \le 4$	$14 \le h \le 14$ $12 \le k \le 12$ $13 \le l \le 7$	$14 \le h \le 14$ $21 \le k \le 19$ $9 \le l \le 15$
Reflections collected	21,941	12,657	7730	13,154
Independent reflections	3545 [R_{int} = 0.0694, R_{sigma} = 0.0839]	2893 [R_{int} = 0.0190, R_{sigma} = 0.0143]	2382 [R_{int} = 0.0507, R_{sigma} = 0.1235]	4910 [R_{int} = 0.0621, R_{sigma} = 0.0783]
Indep. refl. with I ≥ 2σ (I)	1839	2611	1214	3030
Data/restraints/parameters	3545/0/163	2893/0/162	2382/0/163	4910/0/352
Goodness-of-fit on F^2	0.844	1.101	0.768	1.018
Final R indexes [I ≥ 2σ (I)]	R_1 = 0.0402, wR$_2$ = 0.0919[a]	R_1 = 0.0320, wR_2 = 0.0953[b]	R_1 = 0.0396, wR_2 = 0.0637[c]	R_1 = 0.0543, wR_2 = 0.1123[d]
Final R indexes [all data]	R_1 = 0.0876, wR$_2$ = 0.0988	R_1 = 0.0346, wR_2 = 0.0964	R_1 = 0.0864, wR_2 = 0.0672	R_1 = 0.1079, wR_2 = 0.1340
Largest diff. peak/hole/e Å ^{3}	0.25/-0.31	0.28/-0.28	0.32/-0.29	0.50/-0.42
CCDC	2350116	2350117	2350118	2350119

The crystallographic data (excluding structure factors) have been deposited with the Cambridge Crystallographic Data Centre (CCDC) as supplementary publication numbers CCDC-2350116 (**L1**), CCDC-2350117 (**L2**), CCDC-2350118 (**L3**) and CCDC-2350119 (complex **2**). Copies of the data can be obtained, free of charge, by application to CCDC, 12 Union Road, Cambridge, CB2 1EZ, UK (Fax: +44 1223 336033; data_request@ccdc.cam.ac.uk or *via* the internet: http://www.ccdc.cam.ac.uk/products/csd/request.

[a] $w \quad 1/[\sigma^2(F_o^2) + (0.0509\bullet P)^2]$, P $\quad [\max(F_o^2, 0) + 2\bullet F_c^2]/3$.
[b] $w \quad 1/[\sigma^2(F_o^2) + (0.0606\bullet P)^2 + 0.5768P]$, P $\quad [\max(F_o^2, 0) + 2\bullet F_c^2]/3$.
[c] $w \quad 1/[\sigma^2(F_o^2) + (0.0250\bullet P)^2]$; P $\quad [\max(F_o^2, 0) + 2\bullet F_c^2]/3$.
[d] $w \quad 1/[\sigma^2(F_o^2) + (0.0537\bullet P)^2 + 2.8355P]$; P $\quad [\max(F_o^2, 0) + 2\bullet F_c^2]/3$.

*2.2. Syntheses of **L1**–**L3** and complexes **1**–**3***

*2.2.1. General procedure for the synthesis of compounds **L1**–**L3***

To a solution of 2-mercaptobenzimidazole (1.20 g, 8 mmol) in ethanol (50 mL) a solution of KOH (0.45 g, 8 mmol) in ethanol (20 mL) was added and stirred for 1 h at room temperature followed by treatment with a solution of 1,2-, 1,3- or 1,4-*bis*(chloromethyl)benzene (0.70 g, 4 mmol) in ethanol (20 mL). The resulting mixture was refluxed for 24 h. The completion of the reaction was monitored by TLC using *n*-hexane/ethyl acetate (1:1) as eluent. The white precipitate was filtered, washed successively with ethanol and water (each 10 mL) and air dried. Single crystals of **L1**–**L3** suitable for X-ray crystallography were grown from a DMSO/MeOH solution at room temperature *via* slow evaporation method.

L1: Yield: 1.32 g (82 %), mp: 238 °C (dec.); elemental analysis ($C_{22}H_{18}N_4S_2$, 402.52 g/mol) calcd.: C, 65.64; H, 4.51; N, 13.92 %; found: C, 64.80; H, 4.42; N, 12.98 %. IR (KBr, ν, cm ^{1}): 3135 (w, ν N–H imidazole), 3065 (w), 3038(s, ν C—H Ar), 2963 (s), 2930 (w), 2858 (w), 2793 (s), 2632 (w), 2479 (w), 1924 (w), 1882 (w), 1842 (w), 1763 (w), 1618 (s), 1586 (w), 1512 (s, ν C═N), 1442 (s, ν C═C Ar), 1404 (s), 1345 (s), 1266 (s), 1248 (w), 1230 (s, ν C—N), 1209 (w), 1149 (w), 1107 (w), 1079 (w), 1014 (s), 985 (s), 924 (s), 868 (s), 772 (w), 745 (s, ν C—S), 714 (w), 675 (w), 602 (s), 561 (w), 494 (w), 454 (w); ^{1}H NMR (500 MHz, DMSO-d_6, ppm) 4.78 (s, 4H, CH_2), 12.61 (s, 2H, NH), 7.10–7.49 (m, 12H, H—Ar); UV–Vis (DMSO): λ = 303 nm.

L2: Yield: 1.37 g (85 %), mp: 244 °C (dec.); elemental analysis ($C_{22}H_{18}N_4S_2$, 402.52 g/mol) calcd.: C, 65.64; H, 4.51; N, 13.92 %; found: C, 64.90; H, 4.42; N, 12.98 %. IR (KBr, ν, cm ^{1}): 3130 (s, ν N—H imidazole), 3023(s, ν C—H Ar), 2958 (s), 2791 (s), 2695 (s), 2626 (s), 1887 (w), 1766 (w), 1617 (w), 1588 (w), 1512 (s, ν C═N), 1438 (s, ν C═C Ar), 1398 (s), 1265 (s), 1229 (s, ν C—N), 1010 (s), 981 (s), 840 (w), 803 (s), 752 (s), 739 (s, ν C—S), 707 (s), 683 (w), 594 (w); ^{1}H NMR (500 MHz, DMSO-d_6, ppm) 4.54 (s, 4H, CH_2), 12.55 (s, 2H, NH), 7.10–7.55 (m, 12H, H—Ar); UV–Vis (DMSO): λ = 295 nm.

L3: Yield: 1.50 g (93 %), mp: 258 °C (dec.); elemental analysis ($C_{22}H_{18}N_4S_2$, 402.52 g/mol) calcd.: C, 65.64; H, 4.51; N, 13.92 %; found: C, 64.90; H, 4.42; N, 12.98 %. IR (KBr, ν, cm ^{1}): 3129 (w, ν N—H imidazole), 3058(s, ν C—H Ar), 3028 (w), 2965 (s), 2882 (w), 2811 (w), 2721 (w), 2657 (w), 1913 (w), 1879 (w), 1762 (w), 1618 (w), 1585 (w), 1507 (s, ν C═N), 1438 (s, ν C═C Ar), 1394 (s), 1358 (s), 1270 (s), 1227 (s, ν C—N), 1198 (s), 1142 (w), 1098 (w), 1009 (s), 978 (s), 919 (w), 843 (s), 820 (w), 741 (s, ν C—S), 664 (w), 598(s), 521 (s), 496(w); ^{1}H NMR (500 MHz, DMSO-d_6, ppm) 4.57 (s, 4H, CH_2), 12.56 (s, 2H, NH), 7.08–7.45 (m, 12H, H—Ar); UV–Vis (DMSO): λ = 301 nm.

*2.2.2. General procedure for the synthesis of complexes **1**–**3***

A solution of copper(II) sulfate pentahydrate (0.50 g, 2 mmol) in methanol (10 mL) was added to a solution of **L1**, **L2,** or **L3** (0.40 g, 1 mmol) in DMF (10 mL). The resulting mixture was stirred for 24 h at room temperature. The completion of the reaction was monitored by TLC using *n*-hexane/ethyl acetate (1:2) as eluent. The green precipitate was filtered, washed with DMF and methanol (5 mL for each solvent), air dried and used for analyses. Single crystals of complex **2** suitable for X-ray crystallography were grown from the mother liquor (DMF/MeOH

solution) at ambient temperature *via* slow evaporation method.

Complex 1: Yield: 0.68 g (65 %), mp: 240 °C (dec.); elemental analysis ($C_{25}H_{25}CuN_5O_5S_3$, 635.22 g/mol) calcd.: C, 47.27; H, 3.97; N, 11.02 %, found: C, 46.65; H, 3.10; N, 10.56 %. IR (KBr, ν, cm ^{1}): 3144 (w, ν N—H imidazole), 3107 (w, ν C—H Ar), 2984 (w), 2920 (w), 1649 (s, ν C═O DMF), 1497 (s), 1422 (s), 1305 (w), 1278 (s), 1238 (s, ν C—N), 1146 (s), 1107 (w), 958 (s), 937 (w), 814 (w), 760 (s), 660 (s), 597 (s), 576 (s), 497 (w). MS (70 eV) m/z = 404 [**L1** + 1], 466 [**L1** + Cu], 636 [**L1** + $CuSO_4$ + DMF], 657 [**L1** + $CuSO_4$ + DMF+Na^+], UV–Vis (DMSO): λ = 309, 835 nm.

Complex 2: Yield: 0.55 g (87 %), mp: 246 °C (dec.); elemental analysis ($C_{25}H_{25}CuN_5O_5S_3$, 635.22 g/mol) calcd.: C, 47.27; H, 3.97; N, 11.02 %, found: C, 46.80; H, 3.95; N, 10.85 %. IR (KBr, ν, cm ^{1}): 3140 (w, ν N—H imidazole), 3054 (w, ν C—H Ar), 2969 (s), 2920 (w), 1651 (s, ν C═O DMF), 1500 (s, ν C═N), 1433 (s, ν C═C Ar), 1278 (s), 1228 (s, ν C—N), 1134 (s), 1044 (w, ν O=S=O), 1016 (w), 998 (w), 903 (w), 813 (w), 748 (s, ν C—S), 708 (s), 654 (s), 603 (s), 503 (w). MS (70 eV) m/z = 404 [**L2** + 1], 466 [**L2** + Cu], 561 [**L2** + $CuSO_4$], 657 [**L2** + $CuSO_4$ + DMF+Na^+]. UV–Vis (DMSO): λ = 305, 839 nm.

Complex 3: Yield: 0.84 g (80 %), mp: 223 °C (dec.); elemental analysis ($C_{25}H_{25}CuN_5O_5S_3$, 635.22 g/mol) calcd.: C, 47.27; H, 3.97; N, 11.02 %, found: C, 46.91; H, 3.86; N, 10.89 %. IR (KBr, ν, cm ^{1}): 3140 (w, ν N—H imidazole), 3055 (w, ν C—H Ar), 2979 (s), 2914 (w), 2847 (w), 1650 (s, ν C═O DMF), 1507 (s, νC═N), 1419 (s, ν C═C Ar), 1358 (w), 1279 (s), 1228 (w, ν C—N), 1150 (w), 1100 (s), 1055 (w, ν O═S═O), 1020 (w), 999 (w), 815 (w), 741 (s, ν C—S), 653 (s), 585 (s), 502 (s). ESI-MS (70 eV) m/z = 404 [**L3** + 1], 466 [**L3** + Cu + 2], 636 [**L3** + $CuSO_4$ + DMF + 2], 724 [**L3** + 2 $CuSO_4$ + 2], 870 [**L3** + 2$CuSO_4$ + 2DMF + 2], 966 [2**L3** + $CuSO_4$ + 2], 1124 [2**L3** + 2 $CuSO_4$], UV–Vis (DMSO, nm): λ = 306, 833 nm.

2.3. Crystal structure analyses of compounds *L1–L3* and complex *2*

Selected crystals of the compounds were covered with perfluorinated oil and mounted on a STOE StadiVari single-crystal diffractometer (MoK_α radiation, λ = 0.71073 Å, for **L1** and **L3**, GaK_α radiation, λ = 1.34143 Å, for **L2** and CuK_α radiation, λ = 1.54186 Å for **2**), and the crystals were kept at 180 K during data collection. The crystallographic data of **L1**, **L2**, **L3**, and complex **2** are summarized in Table 1. The orientation matrix and the unit-cell dimensions were determined from 9412 reflections for **L1**, 17,955 reflections for **L2**, 2718 reflections for **L3**, and 6563 reflections for **2**. The intensities were corrected for Lorentz and polarization effects. Using Olex2 [69], the structures were solved with the SHELXT [70] structure solution program using intrinsic phasing and refined with the SHELXL [71] refinement package using least squares minimization. Non-hydrogen atoms in all compounds were refined using anisotropic displacement parameters (disordered atoms in **2** were refined isotropically). Hydrogen atom positions of **L1**, **L2** (except H1A) and **L3** were freely refined, whereas H1A of compound **L2** and all hydrogen atoms of complex **2** were calculated in ideal places and refined with a common displacement parameter. For **L2** there were peaks attributed to diffuse/disordered solvent. Attempts to model this were unsuccessful and so the contribution to the diffraction pattern was calculated using the Solvent Mask routine; the electron density was consistent with two molecules of methanol per formula unit. For complex **2**, the coordinated DMF molecule was disordered and was refined over two different orientations (occupancy factor: 0.5:0.5).

2.4. In vitro antibacterial assay

The *in vitro* antibacterial activity of complexes **1**–**3** and their corresponding ligands **L1**–**L3** was evaluated against two pathogenic bacterial strains, including one gram-negative (*Escherichia coli*, ATCC 25922) and one gram-positive bacterial strain (*Staphylococcus aureus*, ATCC 6538), using the plate colony-counting method. The colonies were taken directly from the plate of fresh-cultivated bacteria and were suspended in sterile 0.9 % normal saline. Then, these initial suspensions were adjusted to match the turbidity of a 0.5 McFarland standard (corresponding to the 1.5 10^8 colony forming units (CFU) per mL using 0.05 mL 1.175 % w/v $BaCl_2{\cdot}2H_2O$+99.5 mL 1 % w/v H_2SO_4). The initial suspensions were then 10-fold serially diluted (up to 10^2) in saline (0.9 %). The resulting suspension with a concentration of 1.5 10^6 CFU per mL was also used as the control sample (blank sample). On the other hand, the solutions of all compounds in DMSO (5 mM) were separately prepared by dissolution of **L1**–**L3** (0.010 g, 0.025 mmol) and complexes **1**–**3** (0.016 g, 0.025 mmol) in DMSO (5 mL) and used as test substances (incubation for 24 h at 37 °C). The bacterial suspensions (2 mL) were next spread over the surface of nutrient agar plates containing the test substances (0.5 mL). The plates were incubated at ambient temperature for 24 h. After incubation for 24 h at 37 °C, the samples were 10-fold serially diluted in saline (up to 10^5). 1 mL of each dilution was transferred to agar plates. The number of surviving bacterial colonies (measured in CFUs) was quantitated after cultivation at ambient temperature for 24 h and subsequent incubation of the plates at 37 °C for 24 h.

The rates of colony-forming units (R) were calculated considering the dilution factor using the following equation:

$$R = [(Ncontrol \quad Nsample)/Ncontrol] \times 100\%$$

where N control and N sample are the average number of bacterial colonies of the control sample (containing no antibacterial agent) and the test samples (containing ligand or complex), respectively. All tests were performed in triplicate.

2.5. Cell culture and MTT assay

The human colorectal carcinoma cancer cell lines (*HCT-116*) were grown in culture flasks with RPMI-1640 medium, 10 % fetal bovine serum (FBS), and 1 % antibiotic (streptomycin and penicillin). The culture flask was placed in an incubator with 5 % CO_2/95 % humidity and kept at 37 °C until the cells reached a density of 90 %. The anticancer screening of synthesized ligands and complexes was performed against human colorectal carcinoma *HCT-116* cancer cell line using an MTT assay. For this purpose, plates of 96 wells were filled with 100 mL culture medium containing 5 × 10^3 seeded cells and incubated at 37 °C for 24 h. After medium removal, the cells were treated with the abovementioned compounds in the range of 0–0.3 mM for 48 h. 10 μL of MTT solution was then added to each well and incubated in darkness at 37 °C for 4 h to form formazan crystals. Finally, the media were removed and the formazan crystals were dissolved by the addition of DMSO (100 μL). The absorbance of the supernatant solution was recorded after 20 min at 570 nm using a Microplate Reader (Biotek, USA). The cell viability percentage was determined as follows [72,73]:

$$Cellviability = (OD_{treated}/OD_{control}) \times 100\%$$

where $OD_{treated}$ and $OD_{control}$ are the optical densities of the treated and untreated cells, respectively.

2.6. DAPI staining

The apoptosis induction of carboplatin, and complexes **1**–**3** onto *HCT-116* were determined using DAPI staining for 48 h. The cells were cultured in a 6-well culture plate (5 × 10^4 cells) and treated with CC_{50} values of carboplatin and complexes **1**, **2** and **3**. The cells were then fixed with methanol for 15 min, stained by DAPI (0.2 μg/mL) for 20 min, and washed with PBS. Additionally, the morphology of nuclear cells was observed using fluorescence microscopy (CKX3-SLP, Olympus, Japan).

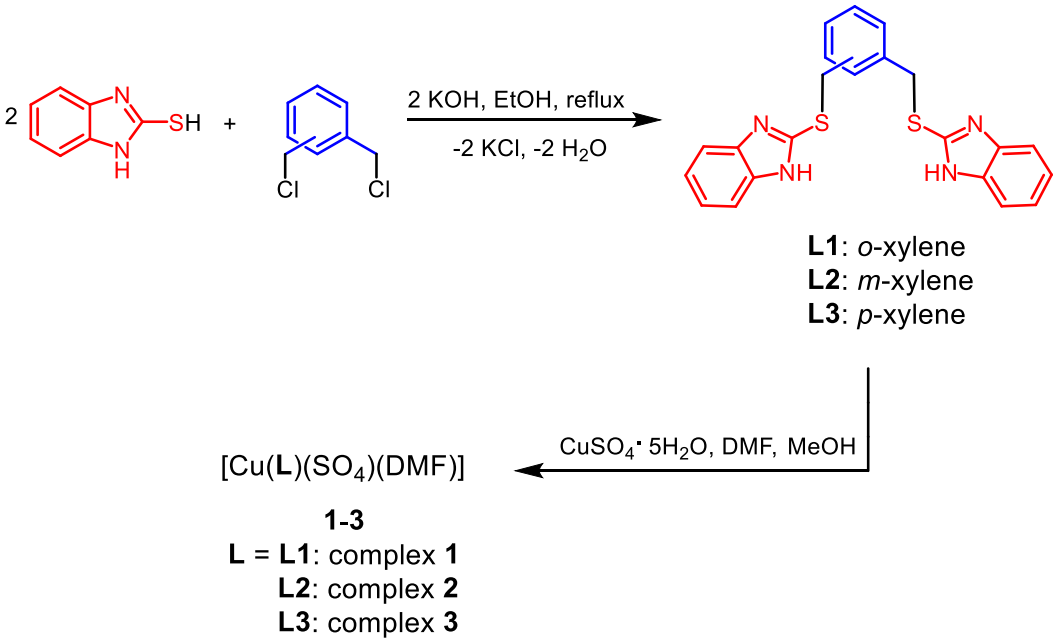

Scheme 2. Synthesis routes of compounds **L1–L3** and their corresponding copper(II) complexes (**1–3**).

2.7. DNA interaction

2.7.1. DNA titration

A solution of 0.55 mL PBS (pH 7.4) containing DNA (0.4 mg/mL) and EB (0.36 mg/mL) was titrated with different concentration of complexes, ranging from 0 to 0.36 mM, at 293 K, 303 K, and 313 K. The excitation wavelength used was 471 nm, and the emission wavelength range was set from 550 to 700 nm. The excitation and emission width slits were both set at 10 nm.

2.7.2. Binding parameters

The Stern–Volmer equation (Eq. (1)) and Hill (Eq. (2)) equation were used to determine the binding parameters as follow [73–75]:

$$F_0/F = 1 + K_{SV}[C] = 1 + k_q\tau_0[C] \quad (1)$$

The fluorescence intensities, F_0 and F, represent the intensities in the absence and presence of the complex, respectively. Where Ksv is a linear Stern–Volmer quenching constant, [C] is the concentration of complexes, kq is the bimolecular quenching rate constant and τ_0 ($\sim 10^{-8}$ s) is the lifetime of the fluorophore in the absence of a quencher. The slope of F_0/F versus [C] plot gives K_{SV}. k_q can be determined using Eq. (1) (ksv = k_q τ).

$$\log(F_0 \quad F)/F = n\log[C] + \log K_b \quad (2)$$

The number of binding sites (n) and binding constant (K_b) was determined from the slope and intercept of log(F_0 F)/F versus log [C] plot.

2.7.3. Thermodynamic parameters

To calculate the enthalpy (ΔH°) and entropy (ΔS°) changes, Van't Hoff equation (Eq. (3)) was used [73].

$$\ln K_b = \quad \Delta H^{\circ}/RT + \Delta S^{\circ}/R \quad (3)$$

where R is the gas constant (8.314 J mol ^{1} K ^{1}) and T is the temperature.

The slope and intercept of ln Kb versus 1/T plot shows ΔH°/R and ΔS°/R, respectively. In addition, the Gibbs free energy (ΔG°) was determined using Eq. (4) [73].

$$\Delta G^{\circ} = \quad RT\ln K_b \quad (4)$$

2.8. Viscosity measurement

To obtain viscosity values of three metal complexes in the interaction with ct-DNA, an Ostwald micro-viscometer was used at 27 °C. The flow time of buffer, the free DNA (60 μM), and various concentrations of all complexes (0, 30, 60, 117, and 173 μM), with a ratio of ri = [complex]/[DNA] = 0, 0.5, 1, 1.95 and 2.9 were measured by digital timing for several times to determine average data [76]. The results were shown graphically as $(\eta/\eta_0)^{1/3}$ versus ratios, where η value for each ratio can be calculated according to the equation: η = (t t_0)/t_0 (t_0 and t are the obtained flow times of free buffer and each DNA-complex solution, respectively) [77]. The η_0 and η parameters are the viscosities of free DNA and complex-DNA, respectively [78].

2.9. Theoretical DFT study

All density functional theory calculations (DFT) were performed using Gaussian09 program (G09) software package [79] using exchange–correlation functionals CAM-B3LYP at room temperature [80]. For DFT calculations, the basis set 6-31G(d) was used for all elements. The geometric structures of **L1**–**L3** in the ground state were fully optimized at RCAM-B3LYP level (restricted CAM-B3LYP). This is while, the geometry optimization of mononuclear copper(II) complex, **1**, (multiplicity 2) and binuclear ones **2** and **3** (multiplicity 3) have been performed at the calcAll CAM-UB3LYP (unrestricted) level of DFT. For compounds **L1**–**L3** and complex **2**, the initial structural models were optimized using their geometries from SC-XRD studies, while the optimization of complexes **1** and **3** were performed on their proposed structures. In order to confirm the stationary structures, vibrational frequencies were calculated by using the analytical second derivatives at the CAM-B3LYP/6-31G(d) level for **L1**–**L3** and calcAll-CAM-B3LYP/6-31G(d) level for copper(II) complexes, **1**–**3**. DFT analysis was carried out to assess the electron transfer from HOMO to LUMO in each compound. Moreover, the energy gap Δ(E_{gap}) between HOMO and LUMO was calculated to evaluate the chemical reactivity descriptors, electrophilic and nucleophilic sites of all synthesized compounds, which are reported as molecular electrostatic potential (MEP) surface photos.

2.10. Docking simulation

Molecular simulation was performed on the optimized geometry of all synthesized compounds. The DNA structure PDB code: 1BNA (5′-D (*CP*GP*CP*GP*AP*AP*TP*TP*CP*GP*CP*G)-3′) was retrieved from the Protein Data Bank (www.rcsb.org/pdb). Program AutoDock 4.2 was used for molecular docking simulations (300 runs). During DNA interaction, various binding energies for all compounds can be followed and the best position of the compound and target with the lowest energy can be selected. All docking simulations were generated using a grid box with 126 × 126 × 126 Å (for 1BNA) points and a grid-point spacing of 0.375 Å. Ultimately, Discovery Studio software (Version 1.15 an) was applied to visualize the DNA-compound interactions [81].

3. Results and discussion

3.1. Synthesis and characterization of *L1–L3* and their parent copper(II) complexes (*1–3*)

Compounds **L1**–**L3** can be obtained as white solids by the reaction of 2-mercaptobenzimidazole and appropriate α,α′-dichloro xylene derivative (*o*-, *m*- and *p*-) in the presence of potassium hydroxide in a molar ratio of 2:1:2 in ethanol. Complexes **1**–**3** can be prepared from the reaction of **L1**–**L3** with copper(II) sulfate pentahydrate in a molar ratio 1:2 in dimethylformamide/methanol as greenish air-stable solids in excellent yields (Scheme 2).

In the ^{1}H NMR spectrum of **L1–L3** recorded in DMSO-d_6 (Figs. SF1–SF3 in supplementary information), the signal corresponding to thioether protons can be observed as a singlet at δ = 4.78 ppm (**L1**) and 4.54 ppm (**L2** and **L3**), whereas those of their aromatic protons appear as multiplet at δ = 7.10–7.55 ppm. Moreover, the signals at δ = 12.61 ppm (for **L1**) and 12.56 ppm (for **L2** and **L3**) can be assigned to NH imidazole protons.

The FT-IR spectra of compounds **L1**–**L3** show a band at 3129–3135 cm ^{1}, which can be assigned to the valence vibrations of NH bonds. Moreover, the characteristic C═N and C—S vibrations can be observed at 1507–1512 cm ^{1} and 739–745 cm ^{1}, respectively (Figs. SF4–SF6(a) in supplementary information). The IR spectra of complexes **1**–**3** exhibit two bands at 3140–3144 and 1497–1500 cm ^{1}, which can be assigned to the valence vibrations of NH and C═N moieties of the coordinated ligands. The observed vibration bands appear to be slightly shifted with respect to the values observed in free ligands pointing out the presence of the **L1**–**L3** as neutral, N-imine donor ligands in the copper complexes. The vibration band observed at about 750 cm ^{1} in the spectra of all complexes can be ascribed to the characteristic vibrations of C—S groups of **L1**–**L3**, whereas those observed at about 670, 960, and 1140 cm ^{1} can be attributed to the stretching and bending modes of the coordinated sulfate dianion. In spectra of complexes **1**–**3**, the vibration bands of C═O group of the DMF molecule appear at about 1650 cm ^{1} [82,83].

ESI-MS spectra of complexes **1**–**3** were recorded in a DMF/methanol mixture (1:2). In all spectra, the peak at *m/z* = 404 [**L**+1] can be assigned to the corresponding ligands **L1**, **L2** or **L3**. Moreover, the peaks at 1051 (complex **1**, Fig. SF7), 657 (complex **2**, Fig. SF8) and 1124 (complex **3**, Fig. SF9) can be attributed to the combinations [2 **L1** + 2 Cu + SO_4 + Na^+], [**L2** + $CuSO_4$ + DMF+1] and [2 **L3** + 2 $CuSO_4$], respectively, confirming the formation of the complexes. Furthermore, peaks corresponding to other fragments are assigned in spectra.

Thermal gravimetric analysis (TGA) of the Cu(II) complexes (**1**–**3**) have been performed in the temperature range of 25–900 °C under an air atmosphere with a heating rate of 10 °C min ^{1}. The thermogram of complexes **1**–**3** are depicted in Supporting Information (Figs. SF10–SF12). The temperature range of decompositions, percentage of weight losses along with the assignments of decomposition moieties of copper(II) complexes are listed in Table ST1. The initial weight losses in the temperature region from 25 to *ca.* 300 °C are associated with the removal of one deoxygenized DMF molecule in complex **1**

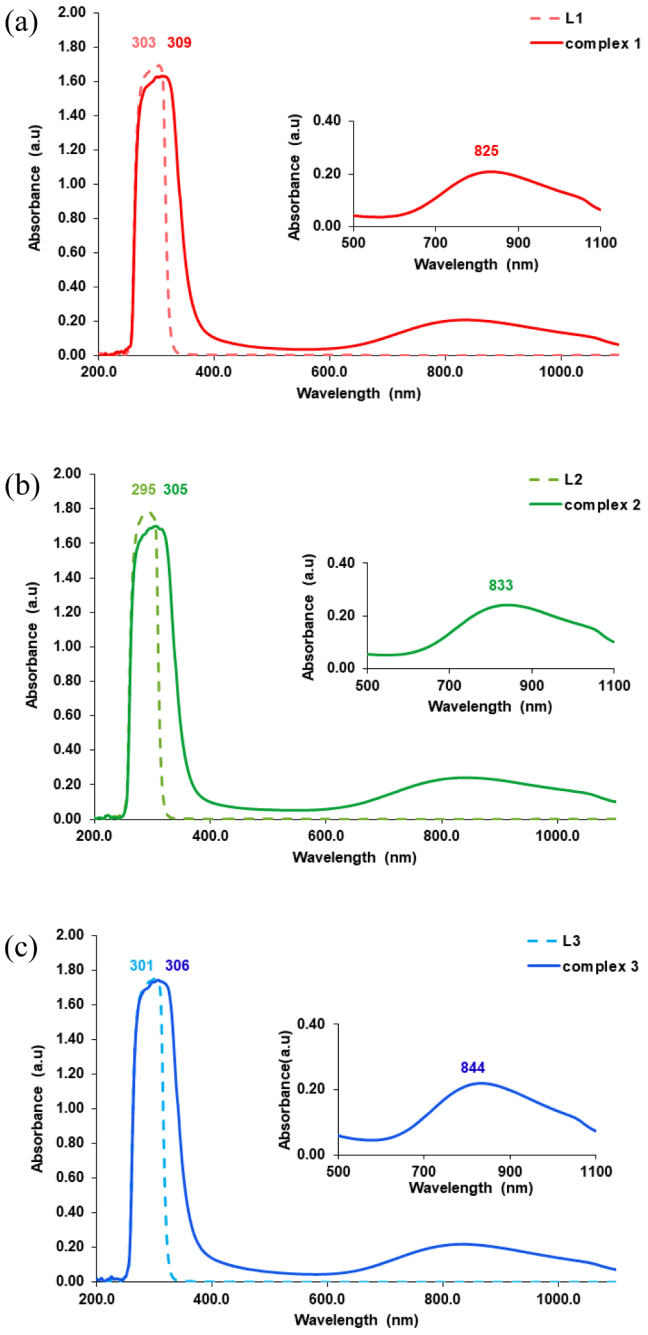

Fig. 1. (a) UV–Vis spectra of compound **L1** (dashed line) and complex **1** (solid line), (b) UV–Vis spectra of compound **L2** (dashed line) and complex **2** (solid line) and (c) UV–Vis spectra of compound **L3** (dashed line) and complex **3** (solid line). The d → d transitions of all complexes are shown in the insets.

(found: 8.44 %; calcd.: 8.97 %), one deoxygenized DMF molecule and one sulfate anion in complex **2** (found: 25.73 %; calcd.: 24.08 %) and one DMF molecule in complex **3** (found: 11.92 %; calcd.: 11.49 %). The weight loss observed in the range of ~300–900 °C may be attributed to the elimination of SO_4 and partly decomposition (liberation) of the $C_{20.5}H_{18}N_4S_2$ fragment of the corresponding ligand for **1** (found: 76.50 %; calcd.: 75.64 %) and total decomposition of **L2** in complex **2** (found: 61.83 %; calcd.: 63.36 %) and elimination of the $C_{20}H_{18}N_4S_2$ fragment in complex **3** (found: 72.11 %; calcd.: 72.17 %). The TG analysis revealed that the thermal degradation process of all complexes at 900 °C leads to the formation of copper(II) oxide. While the final residue of complex **2** consists of pure CuO, those of complexes **1** and **3** are

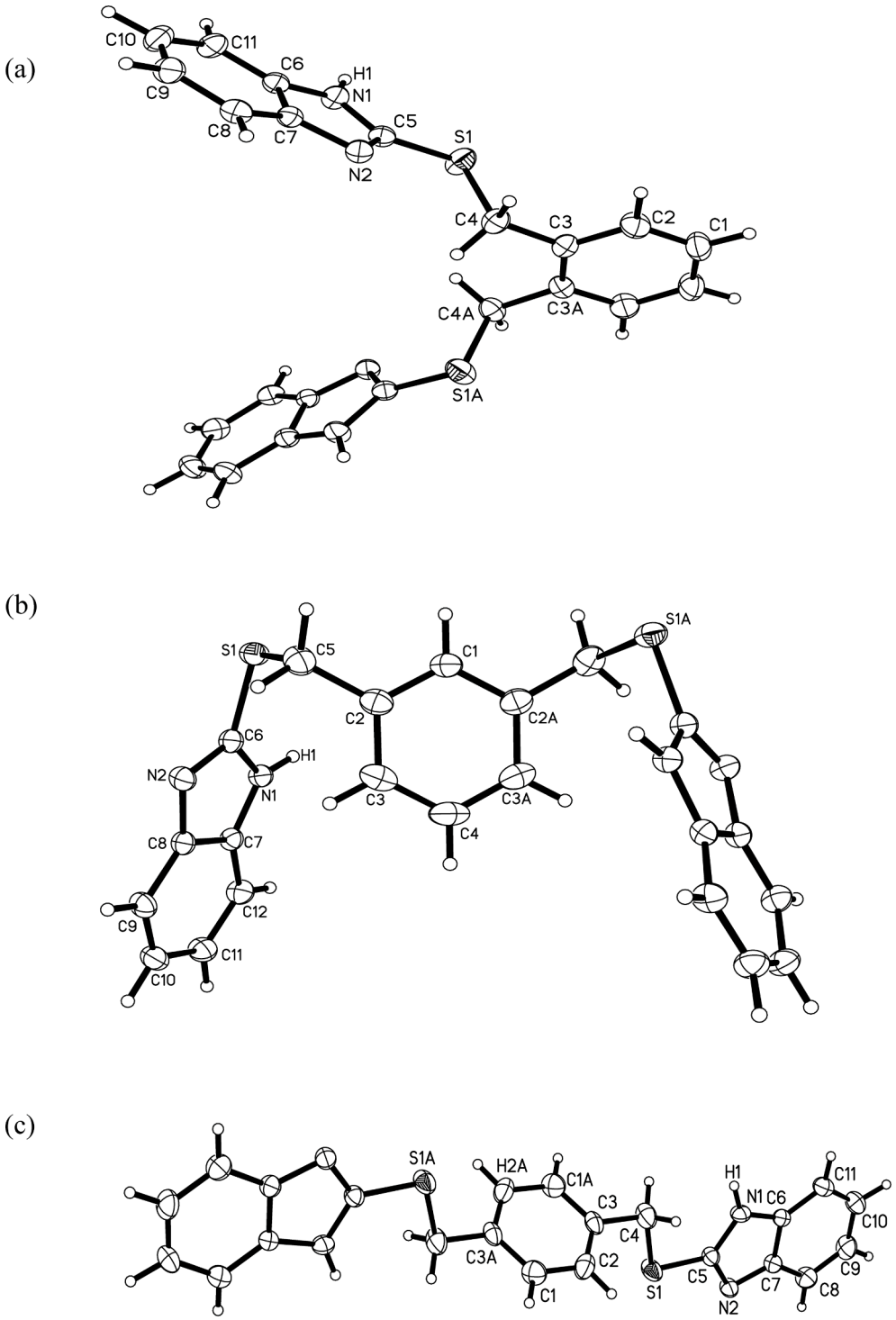

Fig. 2. Molecular structure of (a) **L1**, (b) **L2** and (c) **L3**. Thermal ellipsoids are depicted at 50 % probability level. The symmetry-related atoms were obtained by applying the symmetry code 1 − X, +Y, 0.5 − Z for **L1**, 1 − X, +Y, 0.5 − Z for **L2** and −X, 1 − Y, 1 − Z for **L3**.

contaminated with different amounts of atomic carbon (**1**: found: 15.06 %; calcd.: 15.34 %, **2**: found: 12.44 %, calcd.: 12.56 % and **3**: found: 15.97 %; calcd.: 16.29 %). EDX and P-XRD analyses were performed in order to evaluate the chemical composition of the pyrolysis products of the TGA analyses at 900 °C. The EDX analysis of all residues (Figs. SF13–SF15) evidenced the presence of copper and oxygen and their P-XRD pattern (Fig. SF16) showed solely the characteristic peaks for copper(II) oxide confirming the results of TGA studies.

The UV–Vis spectra of compounds **L1**, **L2,** and **L3** (DMSO solution, 1 $\times 10^{-3}$ M) displayed electronic transitions (ETs) at 303, 295 and 301 nm mainly assigned to the intraligand $\pi \rightarrow \pi^*$ and $n \rightarrow \pi^*$ electronic transitions (Fig. 1a–c). The UV–Vis spectra of complexes **1–3** exhibit intense ETs at 309 nm for complex **1**, 305 nm for complex **2**, and 306 nm for complex **3** showing a slight red shift (≤10 nm) compared to those of their corresponding free ligands. These ETs can be attributed to the intraligand ones and L→M charge transfer transitions. In UV–Vis spectra, the small shift of *ca.* ≤10 nm in the wavelengths of ETs along with the presence of no other ones up to 400 nm indicates that the

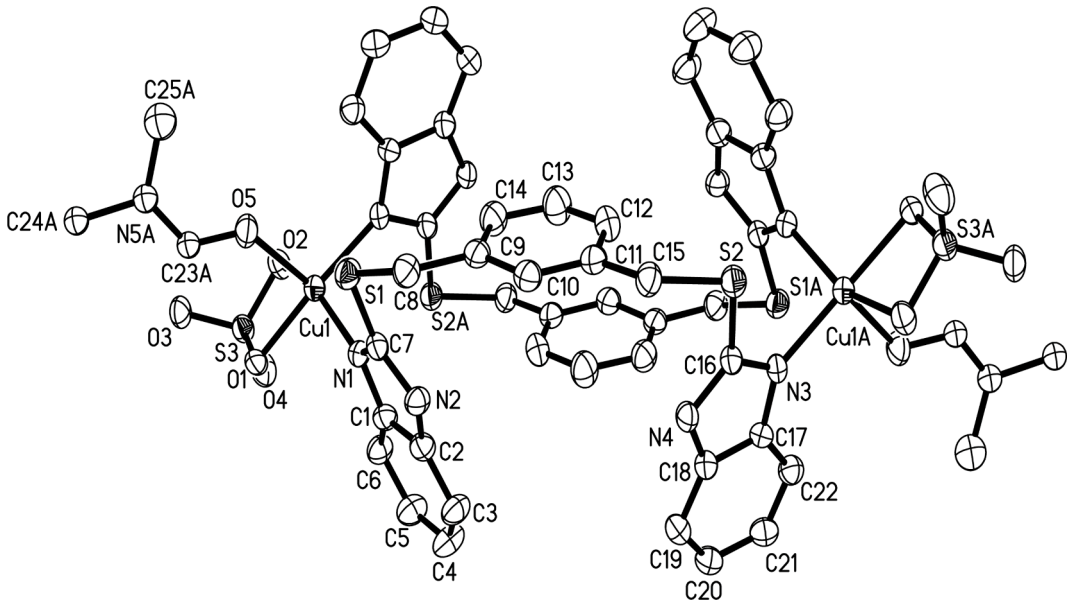

Fig. 3. Molecular structure of complex **2.** Thermal ellipsoids are depicted at the 50 % probability level. Hydrogen atoms and the second disordered component of the DMF molecule were omitted for clarity. The symmetry-related atoms were obtained by applying the symmetry code 1 − X, 1 − Y, 1 − Z.

π-electronic configuration of the corresponding ligand in all complexes (**1**–**3)** remains almost unchanged and hence confirms the coordination of the ligands as a neutral one in these complexes. Furthermore, the broad band of low intensity at 700–1100 nm with a maximum at 835 nm (**1**), 833 nm (**2**), and 844 nm (**3**) can be assigned to the d → d transitions of copper(II) ions indicating the distorted square pyramidal geometry for **1**–**3** (insets in Fig. 1a–c) [83–86].

The results of elemental, mass, and thermal analyses of the copper(II) complexes **1**–**3** revealed that the metal-to-ligand molar ratio in all complexes is 1:1. All complexes are neutral ones including sulfate moieties and dimethylformamide molecules. According to the FT-IR spectra of all complexes, their parent ligands (**L1**–**L3**) are involved in the coordination to metal centers as neutral ligand (presence of NH vibrations). On the basis of these experimental data, the chemical composition for complexes **1**–**3** is suggested as following: $[Cu(\mathbf{L})(SO_4)(DMF)]_n$, in which **L** = **L1**, **L2** or **L3**. This constellation was confirmed for complex **2** by its crystal structure (*vide infra*).

UV–VIS spectroscopy was used to determine the pH effect on the stability of complexes **1**–**3**. The pH-profile (absorbance versus pH) of the synthesized copper(II) complexes is depicted in Fig. SF17. The results obtained in the range pH 1–14 indicated that the complexes are stable and unaffected at pH range of 4–10 for complex **1** and 4–9 for complexes **2** and **3**. In other words, copper(II) complexes **1**–**3** displayed significant stability at determined pH ranges and were therefore well suited for physiological applications [87].

3.2. *Crystal structure descriptions of compounds **L1**–**L3** and complex **2***

The selected bond distances and bond angles of compounds **L1**–**L3**, and complex **2** are given in Table ST2 (Supplementary Information). According to the crystallographic data, compounds **L1**, **L2** and **L3** crystallizes in the centrosymmetric orthorhombic *Pbcn* space group (Z = 4), monoclinic *C2/c* space group (Z = 4) and monoclinic $P2_1/c$ space group (Z = 2), respectively. The structure of each dipodal compounds, **L1**, **L2** and **L3**, consists of two singly deprotonated 2-mercaptobenzimidazole units S-bridged by *ortho*-, *meta*- or *para*-xylene spacer, respectively (Fig. 2a–c).

Compound **L1** has C2 symmetry with a diametrical arrangement of the pendant singly deprotonated 2-mercaptobenzimidazoles displaying an anti-V shape (Fig. 2a). The dihedral angle between the best plane through the xylene ring and the planes through each 2-mercaptobenzimidazole moiety is 71.72°, while both 2-mercaptobenzimidazole pendants are *trans*-positioned (NH groups) and tilted by 64.19° with respect to each other.

In the crystal structure of **L2** (Fig. 2b), the C1 and C4 atoms of the central benzene ring (*meta*-xylene) are located on a crystallographic twofold axis of symmetry (C2). In the non-planar compound **L2**, the thioether spacers are arrayed in a *trans* conformation and the two five-membered imidazole rings (C6 N1 C7 C8 N2) are tilted by 38.38(3)° with respect to each other. The dihedral angle between "best planes" through the central benzene ring (C1 C2 C3 C4 C3 C2) and the plane through each 2-mercaptoimidazole heterocycle is 50.67(5)°. The compound adopts a folded conformation (C6—S1—C5 and S1—C3—C2 angles of 102.92(4)° and 112.39(8)°), and the N—H bonds are oriented in an *anti*-conformation.

In the crystal structure of **L3**, two 2-mercaptobenzimidazole heterocycles are planar and arranged in a *trans* position relative to the central benzene ring, which is located on a crystallographic inversion center (Fig. 2c). The mean plane across each imidazole ring (N2 C7 C6 N1 C5) is inclined to that of central benzene ring (C1 C2 C3 C1 C2 C3) at the angle of 66.47(3)°.

In **L1**, **L2** and **L3**, the C—N, C═N, C—S and C—C bond distances in the five-membered ring of 2-mercaptoimidazole moieties of 1.356(1)–1.396(2), 1.319(2)–1.325(2), 1.739(1)–1.837(1) and 1.401(2)–1.406(1) Å, respectively, are in good agreement with those observed in other S-substituted 2-mercaptobenzimidazoles [88–92]. In **L1**–**L3**, the NH groups of one molecule are connected to the iminic nitrogen atoms of the adjacent one *via* H bonds (N1—H1···N2: 2.812(1) Å and N1—H1—N2: 170.45(2)° for **L1**, N1—H1···N2: 2.831(1) Å and N1—H1—N2: 171.34 (1)° for **L2** and N1—H1···N2: 2.903(3) Å and N1—H1—N2: 158.24(3)° for **L3**). These coordination modes lead to the formation of chains along the crystallographic *c*-axis in all compounds (Figs. SF18–SF20).

Complex **2** crystallizes in the centrosymmetric monoclinic $P2_1/n$ space group (Z = 2). The asymmetric unit of complex **2** consists of a copper ion coordinated by one neutral molecule of **L2**, one sulfate dianion, and one dimethylformamide molecule. In the asymmetric unit, the molecule **L2** acts as a monodentate nitrogen donor ligand, the sulfate dianion as an aniso-bidentate one (as two oxygen donor atoms) and the DMF molecule as a monodentate oxygen donor one resulting in the formation of $[Cu(\mathbf{L2})(\eta^2\text{-}SO_4)(DMF)]$-subunits. Moreover, the

Table 2
Colony numbers and the antibacterial rates for **L1**–**L3**, complexes **1**–**3** and control samples against *E. coli* and *S. aureus* bacterial strains.

Microorganism	Sample	(CFU/mL)	Antibacterial activity (%)
E. coli (ATCC 25922)	**L1**	5.0×10^5	66.66
	complex **1**	1.7×10^5	88.66
	L2	1.4×10^5	90.66
	complex **2**	4.0×10^4	97.33
	L3	1.0×10^5	93.33
	complex **3**	1.5×10^4	99.33
	control	1.5×10^6	–
S. aureus (ATCC 6538)	**L1**	2.2×10^5	85.33
	complex **1**	1.7×10^5	88.66
	L2	1.5×10^5	90.00
	complex **2**	2.0×10^4	98.66
	L3	6.0×10^4	96.00
	complex **3**	1.5×10^4	99.33
	control	1.5×10^6	–

dimerization of these subunits over the second N-imine atom of the dipodal ligand **L2** results in the formation of a centrosymmetric, dimeric binuclear copper(II) complex, $[Cu_2(\mu_2\text{-}\mathbf{L2})_2(\eta^2\text{-}SO_4)_2(DMF)_2]$ (**2**), showing a Cu···Cu separation of 11.747(8) Å (Fig. 3).

In complex **2**, the coordination geometry around each copper(II) ion can be best described as a distorted square pyramidal one since the structural parameter value (τ_5) is 0.13 as defined by Addison *et al.* (N1—Cu1—O2: 152.42(2)°, N3—Cu1—O1: 160.21(2)°, $\tau_5 = 0$ for an ideal square pyramid, and $\tau_5 = 1$ for an ideal trigonal-bipyramid) [57]. In complex **2**, the basal plane of the square pyramidal coordination geometry of each copper(II) ion is formed by two N-imine atoms from two ligands **L2** (N1 and N3) and two oxygen atoms from the sulfate anion (O1 and O2), which has a distorted tetrahedral geometry (O—S3—O angles of 100.65(2)-113.0(2)°). While three bond angles in the N2O2-basal plane (N1—Cu1—N3: 96.62(2)°, N1—Cu1—O1: 92.91 (2)°, and N3—Cu1—O2: 94.33(2)°) deviate (~7°) from the ideal values of a square planar geometry (90°), the major distortion in this plane from the ideal geometry is manifested in the Ol—Cu—O2 chelate angle of 69.95(1)°. The apical position of the square pyramidal geometry is occupied by the oxygen atom of the coordinated DMF molecule (O5; O1—Cu1—O5: 93.50(1)°, O2—Cu1—O5: 95.16(2)°, N1—Cu1—O5: 107.68(2)°, and N3—Cu1—O5: 100.03(2)°). The deviation of the N—Cu—O_{apical} bond angles (107.68(2)° and 100.03(2)°) from the ideal geometry (90°) may be a consequence of the steric hindrance of the two bulky *bis*-benzimidazole ligands. The molecular structure revealed that the copper atom is displaced by 0.335(2) Å from the basal plane toward the apical atom (O5).

Interestingly, the ligand in this complex undergoes a conformational change (from *anti* conformation in free ligand to *syn* conformation with respect to NH groups of its benzimidazole moieties) upon metalation with copper(II) ions. The flexibility of the dipodal ligand is well demonstrated by the changes in the values of the dihedral angles formed by the benzimidazole rings and the central benzene ring of 81.02(7)°, 82.63(7)°, and 77.26(5)° with regard to those observed in free ligand (vide supra).

In this complex, the Cu—N bond distances of mean 1.989 Å are in good agreement with those observed in other copper(II) complexes bearing imidazole derivatives [93–101]. In addition, the bond lengths and angles within the 2-mercaptobenzimidazole moieties remain unchanged with respect to those in the parent ligand. The equatorial Cu—O bond lengths of 2.008(3) Å and 2.039(3) Å are in the range observed in copper(II) complexes bearing an aniso-bidentate sulfate anion [102]. The apical Cu1—O5 bond length of 2.136(4) Å is somewhat longer than the equatorial bond lengths and has a similar value as observed in dimeric copper(II) complexes incorporating apical coordinated DMF molecules $[Cu(HCOO)_2(DMF)]_2$ (Cu—O_{apical}: 2.131(3) Å) [103] and $[Cu(taa)_2(dmf)]_2$ (taa = 2-thiopheneacetate anion, Cu-O_{apical}: 2.141(2) Å) [104].

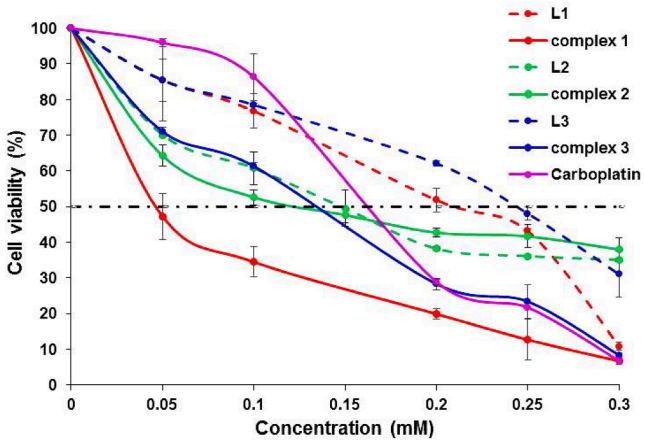

Fig. 4. Cell viability percentages of *HCT-116* with increasing concentration of compounds **L1**–**L3**, copper(II) complexes **1**–**3** and carboplatin.

Furthermore, in complex **2**, each sulfate ion acts as a bridging agent between two NH groups of benzimidazole moieties of two adjacent binuclear complexes *via* intermolecular hydrogen bonds (N2—H2···O2b: 2.753(2) Å and N2—H2—O2b: 159.46(6)°, N4—H4···O3b: 2.757(2) Å and N4—H4—O3b: 166.85(7)°). These interactions might be responsible for further stabilization of complex **2** (Fig. SF21).

3.3. Biological activity

3.3.1. In vitro antibacterial activity

The *in vitro* antibacterial activities of compounds **L1**–**L3** and their corresponding copper(II) complexes **1**–**3** were tested against two pathogenic bacterial strains involving one gram-negative (*Escherichia coli ATCC 25922 PTCC 1399*) and one gram-positive bacterial strain (*Staphylococcus aureus ATCC 6538 PTCC 1112*). The samples were incubated at 37 °C for 24 h and the results of the biological investigations are summarized in Table 2. According to these results, compounds **L1** and **L3** showed a higher antibacterial activity against the gram-negative bacterial strain (85.33 % and 96.00 %, respectively) than the gram-positive one (66.66 % and 93.33 %, respectively). This is while **L2** displays similar antibacterial effectiveness against both bacterial strains (90.66 % and 90.00 % against gram-negative and gram-positive bacterial strains, respectively). The test results indicated that the antibacterial activity of **L1**–**L3** against both bacterial strains decreased in the order of **L3** > **L2** > **L1**. Moreover, the results revealed that complexes **1**–**3** showed similar rates of antibacterial activity against both bacterial strains. The antibacterial activity of the ligands against both bacterial strains increased upon coordination to the metal center, and complexes **1**–**3** showed the same order in terms of antibacterial activity (**3** > **2** > **1**) as their parent ligands.

3.3.2. In vitro cytotoxic activity

The cytotoxicity of the synthesized compounds **L1**–**L3** and their corresponding complexes **1**–**3** was evaluated against the human colorectal carcinoma cancer cell line (*HCT-116*) using an MTT toxicity assay. The results revealed that the cell viability percentage decreased with increasing concentrations in the range of 0–0.3 mM; hence, the cancer cell line viability of the tested compounds turned out to be dose-dependent. The anticancer screening of the tested compounds revealed that the cytotoxic concentration values for the death of 50 % of viable cells (CC_{50}) were 0.210, 0.150, and 0.240 mM for **L1**, **L2**, and **L3**, respectively. This is while, the CC50 for their corresponding copper(II) complexes were 0.045 mM for **1**, 0.110 mM for **2**, and 0.135 mM for **3**. Moreover, the data were compared with carboplatin as a standard anticancer drug under the same conditions (Fig. 4). The results revealed

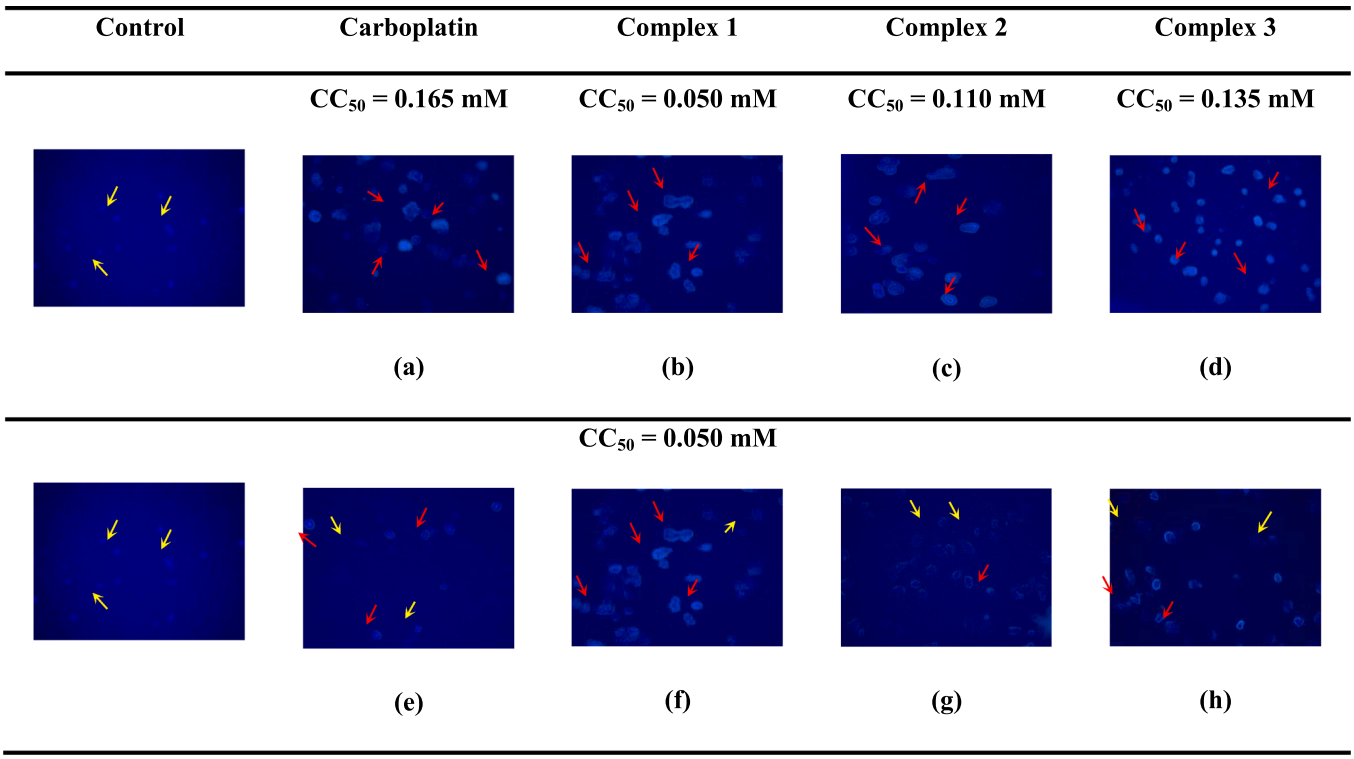

Fig. 5. DAPI staining of control, carboplatin and complexes **1–3** onto treated *HCT-116*.

that all copper complexes **1**–**3** displayed higher *in vitro* anticancer activities toward this cancer cell line than their free ligands, **L1**–**L3**, and carboplatin (CC_{50} = 0.165 mM). The comparison of cytotoxicity between ligands and carboplatin against *HCT-116* cell lines revealed that only **L2** exhibited greater anticancer activity than carboplatin. Amongst the synthesized complexes, complex **1** exhibited the highest cytotoxicity (CC50: 0.045 mM), which was comparable with that of copper(II) complexes $Cu_2(bpbib)_2(BF_4)_2Cl_2$ and $[Cu(p\text{-}4\text{-}bmb)(Ac)_2]_2$ incorporating *bis*-benzimidazole ligands displaying CC50 values of 0.049 mM and 0.056 mM, respectively (bpbib = 1,4-*bis*((2-(pyrazin-2-*yl*)-1*H*-benzo[d]imidazol-1-*yl*)methyl)benzene, *p*-4-bmb = 1-((2-(pyridin-4-yl)-1*H*-benzoimidazol-1-*yl*)methyl)-*1H*-benzotriazole) [105,106].

Therefore, the results indicate that compound **L2** and complexes **1**–**3** may be promising candidates as antitumor agents against human *HCT-116* colorectal cancer cells.

3.3.3. Morphological assessments

DAPI (4′,6-diamidino-2-phenylindole) is a fluorescent probe that binds to DNA and is commonly used in biology and microscopy to stain and visualize the nucleus of cells. It emits blue fluorescence when excited by ultraviolet light. Additionally, DAPI binds to the minor groove of double-stranded DNA, and its high affinity and specificity for DNA have rendered it a popular choice for staining. Furthermore, DAPI is employed to differentiate between live and dead cells since it is unable to penetrate the membrane of intact cells. The control cells display an oval-shaped nuclei with smooth edges, whereas the apoptotic cells appear with a condensed and fragmented nucleus [107,108]. Therefore, DAPI staining of the nucleus can aid in distinguishing between cells with intact and compromised membranes [109].

The results of DAPI staining for the treatment of *HCT-116* cells at CC_{50} values of carboplatin and all complexes after 48 h are shown in Fig. 5a–d. In addition, to compare the morphology of cells in the same concentration of complexes, the lowest CC_{50} value of 0.050 mM related to complex **1** was selected (Fig. 5e–h). The normal nuclei are blue with a round shape and sharp edge (Fig. 5, yellow arrow), whereas the shrunken and fragmented nuclei show the cell death (Fig. 5, red arrow). The first row clearly indicates the change in the morphology of cells demonstrating cell death, whereas the pictures in the second row indicate that cell death occurred entirely in complex **1** and that the other complexes caused moderate shrinkage in cells. The comparison of morphology of treated cells with carboplatin and complexes **1**–**3** indicates that apoptotic induction of these complexes is significantly greater than that of carboplatin due to shrunken and fragmented nuclei in treated cells with carboplatin. Consequently, the designed complexes showed more effectiveness with low cytotoxicity and apoptotic induction on *HCT-116* cells than carboplatin.

3.3.4. DNA interaction

– *Competitive binding*

The binding affinity of the complexes to DNA has been studied by displacement of EB probe as a well-known DNA intercalator. The EB probe produces strong fluorescence when it intercalates into DNA. Therefore, if a non-fluorescent molecule binds to the DNA.EB complex and displace the intercalated EB, it will result in a reduction in fluorescence intensity, known as quenching [66,67,73]. In this study, the quenching behavior of DNA was examined by recording the maximum fluorescence emission of DNA pre-treated with EB upon addition of complexes **1**–**3**. As depicted in Fig. 6, the fluorescence intensity of DNA. EB decreased as the concentration of complexes increased, which confirmed the replacement of EB molecules with complexes and the interaction between DNA and the complexes. Consequently, further investigations were conducted to determine the mode and strength of DNA binding affinity of the complexes, including the determination of binding and thermodynamic parameters.

– *Binding parameters*

The fluorescence quenching mechanism can be divided into two types: static and dynamic, which are temperature-dependent. Dynamic quenching occurs when the excited fluorophore collides with the

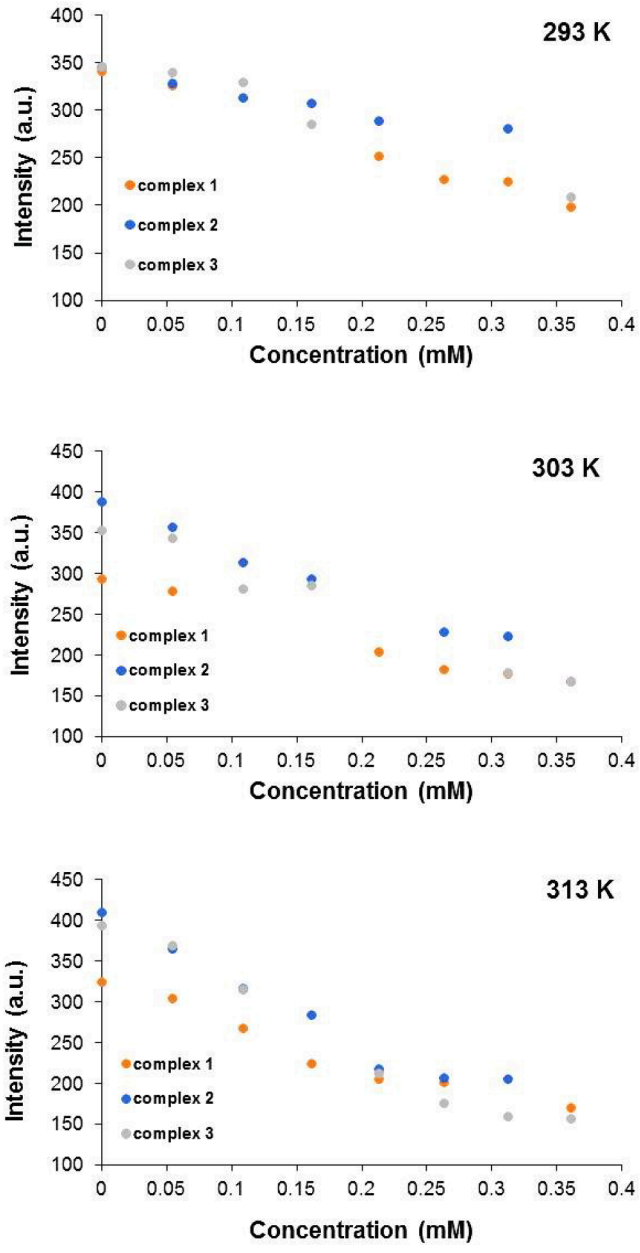

Fig. 6. The maximum fluorescence intensity changes of DNA.EB with the addition of different concentrations of complexes **1**–**3** at 293 K, 303 K, and 313 K.

quencher molecule, and results in a higher quenching constant at higher temperatures. On the other hand, static quenching involves interactions between the fluorophore and quencher in the ground state, and an increase in the temperature leads to a decrease in the quenching constant [73,74]. The binding parameters were determined according to Eqs. (1) and (2) (Table 3, Figs. SF22 and SF23). K_{SV} values of complexes **1**–**3** in their interaction with DNA.EB increased with higher temperatures, indicating a dynamic quenching process. The determined values of k_q are lower than 2.0×10^{12} M^{-1} s^{-1} to further confirm the dynamic quenching mechanism [73,74]. These results were consistent with the findings mentioned above.

Furthermore, the binding constant and number of binding sites in the interaction process increased with higher temperatures, suggesting an increased affinity of binding. Moreover, the binding parameters of DNA in its interaction with complex **3** were greater than those of complexes **1** and **2**, which can be attributed to the structural characteristics of complex **3** that favor the binding process.

– *Thermodynamic parameters*

The mode of binding force between biomolecules and small molecules was evaluated by determining thermodynamic parameters. Ross and Subramanian demonstrated that non-covalent bindings of hydrogen, *van der Waals*, electrostatic, and hydrophobic forces play significant roles in the interaction process. The negative values of ΔH and ΔS indicate that the two main forces involved in the complex are hydrogen bonds and *van der Waals* force. This is while a small or zero value of ΔH and positive value of ΔS are associated with electrostatic forces and positive value of ΔH and ΔS are commonly taken for hydrophobic interactions [73]. The results from Fig. SF24 and Table 3 show positive values for enthalpy and entropy pointing out the fact that hydrophobic binding plays a major role in the interaction process.

3.3.5. *Viscosity measurements*

To obtain a deeper insight on the nature of interaction between the synthesized copper(II) complexes and DNA, viscosity measurements have been carried out. Viscosity measurements are hydrodynamic methods used as one of the most effective routes for studying the binding mode of compounds to DNA due to the fact that these measurements are sensitive to any change in DNA length [77].

Intercalation and groove binding are two of the most observed binding modes between compounds and DNA. In the traditional intercalative mode, the interaction between the compound and DNA leads to an increment in DNA viscosity as a consequence of the overall DNA lengthening caused by the segregation of base pairs at the intercalation site. In contrast, the second binding mode (groove binding) shows negligible change in the viscosity of the DNA solution.

The results of the viscosity measurements of all synthesized complexes and EB with DNA are shown in Fig. 7. In contrast to the interaction of EB with DNA (formation of intercalation mode), those of the

Table 3
Binding and thermodynamic parameters of interaction between DNA.EB and complexes **1**–**3.**

	T (K)	K_{SV} ($\times 10^3$ M^{-1})	k_q ($\times 10^{11}$ M^{-1} s^{-1})	R^2	K_b ($\times 10^3$ M^{-1})	n	R^2	ΔG (kJ/mol)	ΔH (kJ/mol)	ΔS (kJ/mol.K)	R^2
Complex 1	293	1.95	1.95	0.97	3.26	1.48	0.99	19.70	10.42	0.10	0.99
	303	2.23	2.23	0.99	3.70	1.41	0.99	20.70			
	313	2.59	2.59	0.98	4.28	1.37	0.97	21.76			
Complex 2	293	0.76	0.76	0.97	1.50	0.86	0.98	17.82	47.00	0.22	0.98
	303	2.55	2.55	0.98	3.33	1.23	0.99	20.43			
	313	3.63	3.63	0.95	5.13	1.28	0.97	22.23			
Complex 3	293	1.92	1.92	0.97	5.55	2.00	0.97	21.00	26.77	0.16	0.98
	303	3.29	3.29	0.95	8.65	1.88	0.93	22.84			
	313	4.78	4.78	0.97	11.17	1.74	0.99	24.26			

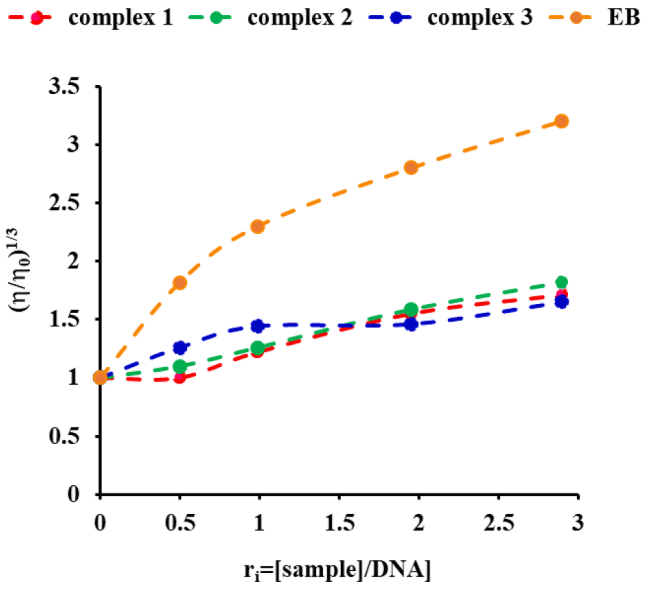

Fig. 7. The viscosity changing of DNA by titrating various concentrations of each Cu complex and EB as an intercalator agent.

synthesized complexes with DNA led to a minor change in DNA conformation. These results indicate that all copper(II) complexes interact with DNA *via* groove binding. The experimental results are in agreement with those reported in the theoretical docking studies (*vide infra*).

3.4. Computational study

3.4.1. Optimized structures

The X-ray crystal structures of the compounds **L1**–**L3** and complex **2** were used as initial geometries in DFT optimization calculations. Complexes **1** and **3** were not structurally characterized and full optimization of these complexes was performed on their proposed structures [Cu**L1**(SO_4)] and [Cu**L3**(SO_4)(DMF)]$_2$. The structures of **L1**–**L3** were optimized at RCAM-B3LYP/6-31G(d) level, whereas those of copper(II) complexes were done at calcAll-CAM-B3LYP/6-31G(d) level. The stationary points were identified as positive on the potential energy surface showing no imaginary frequencies for the 3N 6 vibrational degrees of freedom (N is the number of atoms in the system). Calculated energies of optimized geometries and other physical parameters for all compounds are listed in Table ST3. The DFT data represent similar values of total energy of 50721.77 eV (**L1**), 50722.05 eV (**L2**) and 50721.50 eV (**L3**) with dipole moment of 0.41, 1.16 and 0.00 Debye(s) for **L1**, **L2** and **L3**, respectively. Moreover, the DFT results revealed that these compounds are stabilized upon complexation with the metal ions. The calculated total energy value of mononuclear copper(II) complex **1** was found to be 121139.43 eV, while those of complexes **2** and **3** were 242279.14 eV and 242279.96 eV, respectively. The optimized parameters (bond lengths and bond angles) of all synthesized compounds are listed in Table ST2. The DFT results indicated that the calculated parameters of **L1**–**L3** and complex **2** are in good agreement with the crystallographically determined ones. The calculated geometry index (τ_5) of 0.13 for complex **2** from optimized data corroborates the crystallographically characterized square pyramidal geometry around each copper ion in this complex.[57] The calculated geometry index (τ_5) of 0.21 for complex **1** and 0.18 for complex **3** (from their optimized structure) allows us to suggest the distorted square pyramidal geometry for copper ion(s) in these complexes. The optimal geometry of the synthesized compounds is depicted in Fig. 8a–f.

The small difference within the experimental and theoretical values is traced back to the fact that the theoretical calculations were done in the gas phase, whereas experimental data were determined from the solid phase [110].

3.4.2. Infrared vibration calculations

The validity of the proposed structure for the synthesized compounds (**L1**–**L3** as well as complexes **1**–**3**) was examined on the basis of their experimental and theoretical vibrational frequencies. The hybrid CAM-B3LYP/6-31G(d) basis set has been employed to calculate the infrared vibrations of compounds **L1**–**L3** consisting of 46 atoms with C2 symmetry for **L1** (46 normal vibration modes) and C1 symmetry for **L2** and **L3** (132 normal vibration modes). This is while, the infrared vibrations of copper(II) complexes were calculated with the hybrid set calcAll-CAM-B3LYP/6-31G(d). The results revealed 186 normal vibration modes for the mononuclear copper(II) complex **1** consisting of 64 atoms (C1 symmetry). Besides, 378 normal vibration modes were observed for each binuclear copper(II) complexes **2** and **3** with 128 atoms (C1 symmetry). It is noteworthy to mention that the calculated vibration frequencies are usually higher than those observed from experimental data. This difference is traced back to the fact that the calculations are performed for a single molecule in the gas phase, while experimental measurements take place in the solid state in the presence of intermolecular interactions. Therefore, to gain a better comparison between these data, the theoretical wavenumber values have been scaled by scaling factor of 0.952 [111]. The experimental infrared spectra of **L1**–**L3** and complexes **1**–**3** and the calculated ones (unscaled as well as scaled) are illustrated in Figs. SF4a–6a. Indeed, the real IR-relation in compounds can be determined from the graphical correlation between the experimental and calculated vibration frequencies. The determined R^2 values of these data are found to be 0.999 (**L1**, **L3** and complex **3**) and 0.998 (**L2**, complexes **1** and **2**) demonstrating a high degree of agreement between these data and confirm the proposed structure of the synthesized compounds (Figs. SF4(b,c)–SF6(b,c)).

3.4.3. Frontier molecular orbital energy (FMO) and quantum chemical descriptors

The Frontier molecular orbital theory (FMO) based on the highest occupied molecular orbital (HOMO) and lowest unoccupied molecular orbital (LUMO) is one of the most used theories in order to explain the chemical reactivity of a molecule [112]. The HOMO and LUMO energies of a compound provide information about its ability to donate and accept electron, respectively. Additionally, the negative magnitude of HOMO and LUMO energies explains the stability of the compound. Moreover, the HOMO and LUMO energy difference (ΔE_{gap}) is a measure to indicate the chemical reactivity and kinetic stability, optical polarizability and chemical hardness–softness of molecular systems. According to the structural arrangement and electronic distribution of the optimized compounds, the charge of all compounds is zero. The ground state of the structures have been optimized with singlet multiplicity for **L1**–**L3** at CAM-B3LYP/6-31G(d) level, doublet one for the mononuclear copper(II) complex **1** (unrestricted, α- and β-MO) and triplet one for both binuclear copper(II) complexes **2** and **3** (unrestricted, α- and β-MO) at calcAll-CAM-B3LYP/6-31G(d) level. The molecular orbital energy diagram (HOMO and LUMO densities) of each copper(II) complex along with that of its related ligand is illustrated in Fig. 9. Diagrams in Fig. 9a–c revealed that the HOMO orbitals in compounds **L1**–**L3** are mainly distributed across their both 2-mercaptobenzimidazole rings. The LUMO orbitals in **L1** and **L3** are concentrated on their central benzene ring, whereas those in **L2** are localized over 2-mercaptobenzimidazole and benzene ring orbitals. According to the HOMO-LUMO diagram of complex **1** (unrestricted, α- and β-MOs), the HOMO orbitals are located on its sulfate ions, metal center and thioetheric sulfur atom in its α-MO and on 2-mercaptobenzimidazole moiety and sulfate group in its β-MO. On the other hand, the LUMO orbitals are distributed over the benzene ring and 2-mercaptobenzimidazole group in the α-MO and over the metal center, sulfate moiety and iminic nitrogen atom in the β-MO. Moreover, the binuclear complexes **2** and **3** show similar

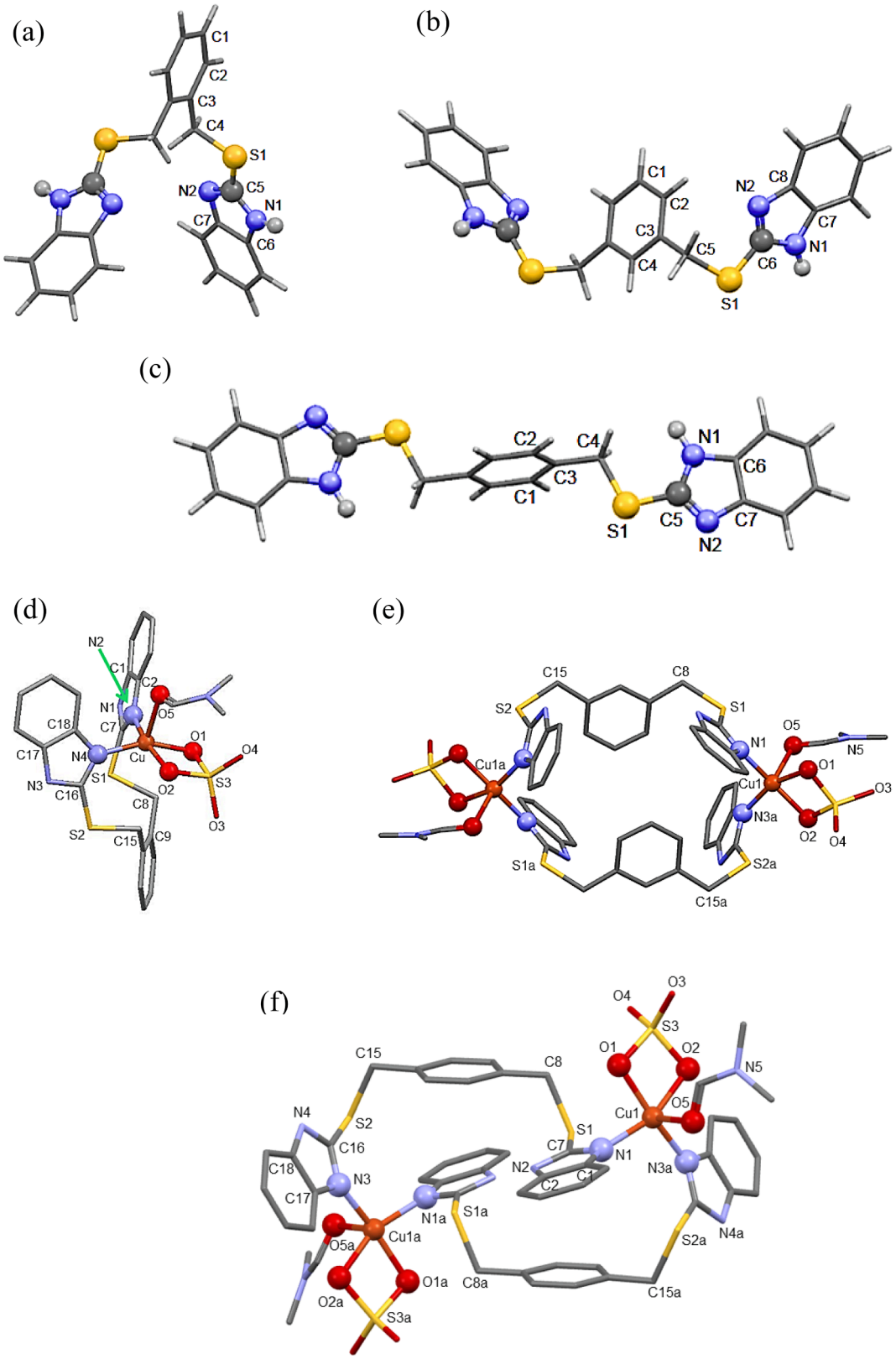

Fig. 8. Optimized structure of (a) **L1,** (b) **L2**, (c) **L3**, (d) complex **1**, (e) complex **2** and (f) complex **3** (Hydrogen atoms of complexes are hidden for clarity).

orbital distributions in their HOMO and LUMO levels. Their HOMO orbitals are distributed over their sulfate group, metal center and iminic nitrogen atoms of the benzimidazole units, whereas their LUMO orbitals are concentrated on their aromatic benzene and benzimidazole rings.

The determined HOMO and LUMO energies of all compounds are listed in Table 4. The determined energy gap (ΔE_{gap}) revealed that **L2** with 7.780 eV is the most stable compound amongst **L1**–**L3** and the stability of ligands decreased in following order: **L2** > **L1** > **L3**. According to the frontier molecular orbital diagrams, the both HOMO and LUMO levels of complexes **1**–**3** are downshifted, which led to the

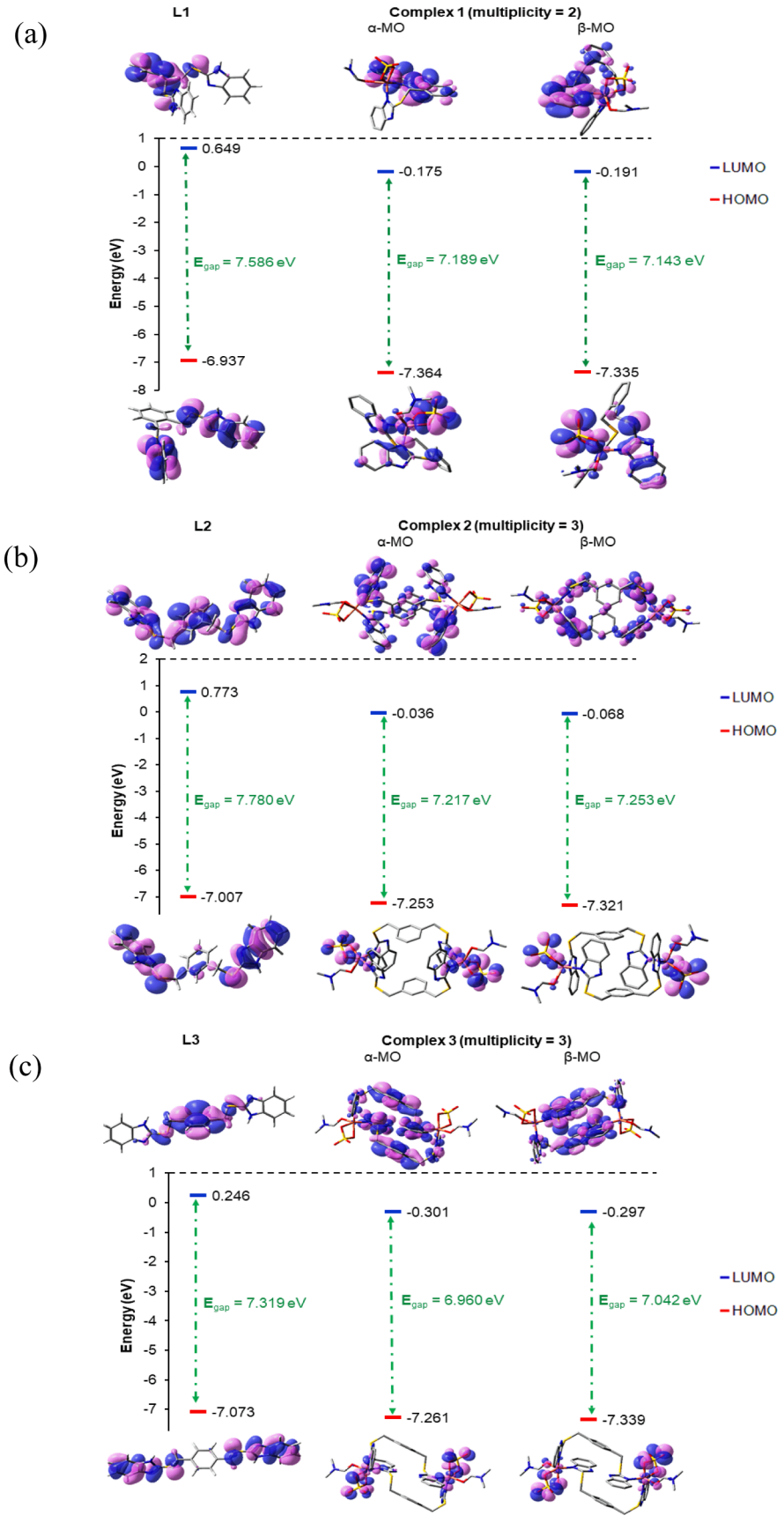

Fig. 9. Schematic of HOMO and LUMO frontier molecular orbital densities (a) for **L1** and complex **1**, (b) for **L2** and complex **2** and (c) for **L3** and complex **3** (hydrogen atoms in all complexes are omitted for clarity).

Table 4
Determined HOMO and LUMO energies and calculated quantum chemical descriptors of **L1**–**L3** and copper(II) complexes **1**–**3.**

	L1	**L2**	**L3**	**Complex 1**		**Complex 2**		**Complex 3**	
				Spin: doublet		Spin: triplet		Spin: triplet	
E_{total} (Hartree)	1863.99	1864.00	1863.98	4451.79		8903.59		8903.62	
E_{total} (eV)	50721.79	50722.06	50721.52	121139.47		242279.22		242280.03	
				α MOs	β MOs	α MOs	β MOs	α MOs	β MOs
HOMO (Hartree)	0.255	0.258	0.260	0.271	0.270	0.267	0.269	0.267	0.270
HOMO (eV)	6.937	7.007	7.073	7.364	7.335	7.253	7.321	7.261	7.339
LUMO (Hartree)	0.024	0.028	0.009	0.006	0.007	0.001	0.003	0.011	0.011
LUMO (eV)	0.649	0.773	0.246	0.175	0.191	0.036	0.068	0.301	0.297
I = (HOMO)	6.937	7.007	7.073	7.364	7.335	7.253	7.321	7.261	7.339
A = (LUMO)	0.649	0.773	0.246	0.175	0.191	0.036	0.068	0.301	0.297
$E_{GAP} = (E_{LUMO}-E_{HOMO})$	7.586	7.780	7.319	7.189	7.143	7.217	7.253	6.960	7.042
$\eta = (I \quad A)/2$	3.793	3.890	3.659	3.595	3.572	3.608	3.626	3.480	3.521
$\sigma = (1/\eta)$	0.264	0.257	0.273	0.278	0.280	0.277	0.276	0.287	0.284
$\chi = (I + A)/2$	3.144	3.117	3.413	3.770	3.763	3.645	3.694	3.781	3.818
CP = χ	3.144	3.117	3.413	3.770	3.763	3.645	3.694	3.781	3.818
$\omega = (CP^2/2\eta)$	1.303	1.249	1.592	1.977	1.982	1.841	1.882	2.054	2.070
$N = (1/\omega)$	0.767	0.801	0.628	0.506	0.504	0.543	0.531	0.487	0.483
$\Delta N_{max} =$ (CP/η)	0.829	0.801	0.933	1.049	1.054	1.010	1.019	1.086	1.084
$S = (1/2\eta)$	0.132	0.129	0.137	0.139	0.140	0.139	0.138	0.144	0.142

decrement of ΔE_{gap} in these complexes with respect to their related free ligands (7.166 eV for **1**, 7.235 eV for **2** and 7.001 eV for **3**). The results indicate that all complexes are chemically more reactive than their ligands since the lower the energy gap the easier the transition between frontier orbitals of the molecule and the greater chemical reactivity [112,113]. Moreover, the frontier orbital studies of a molecule provides also insight in its quantum chemical descriptors, namely, hardness (η), softness (σ), electrophilicity index (ω), chemical potential (CP), and electronegativity (χ), which are useful parameters to predict its chemical reactivity, kinetic and thermodynamic stability. The calculated data for quantum chemical descriptors are given in Table 4. Larger HOMO-LUMO energy gaps are associated with higher global chemical hardness, which results in harder molecules, higher stability and lesser chemical reactivity. The determined values indicated that the stability and hardness of studied compounds decreased in the order **L2** > **L1** > **L3** for free ligands and in the order **2** > **1** > **3** for copper(II) complexes. The global electrophilicity index (ω) may be considered as the most important quantum chemical descriptor playing a crucial role in the determination of the chemical reactivity of molecular systems. This index represents the decrease in energy caused by the flow of electrons from HOMO (donor) to LUMO (acceptor) orbitals in molecules and is directly proportional to square of the electronic CP of a system and reciprocally proportional to its global chemical hardness (η). The electronic chemical potential gives information about the charge transfer of a system in its ground state. The negative value of CP indicates the stability of a compound and suggests that it does not decompose into elements. Thus, compounds with higher CP are more reactive than those with small ones. According to the calculated data, the **L2** among **L1**–**L3** and complex **2** among **1**–**3** are the most reactive ones. The reactivity of all ligands and complexes decreased in the order **L2** > **L1** > **L3** > **2** > **1** > **3**. Furthermore, the electronegativity (χ) is introduced as the ability and power of an atom in a compound to attract electrons to itself in a covalent bond. The calculated values of electronegativity revealed that **L3** and complex **3** have higher electronegativities and are strongly electrophilic, while **L2** and complex **2** showing the lowest values of electronegativity are nucleophilic. Finally, due to the determined values of ΔE_{gap} energies and global hardness and other quantum chemical descriptors, the stability of the studied compounds decreased in the order **L2** > **L1** > **L3** > **2** > **1** > **3** in the gas phase, whereas their chemical reactivity decreased in the opposite order.

The quantum parameters calculated for the optimized structures of all synthesized compounds has led to the following important results:

(i) All free ligands are more stable than copper(II) complexes due to their higher ΔE_{gap} value, higher nucleophilicity and lower electrophilicity.
(ii) The chemical activity of the ligands is higher than complexes because of their lower χ and higher CP values and hence they will easily give electrons in the complex state.
(iii) The decrease of ΔE_{gap} values demonstrate that all complexes exhibit high biological activity compared to free ligands.
(iv) The biological activity of all complexes is higher than their related ligands due to their greater ΔN_{max} and global softness (S) values as well as their higher electrophilicity and lower nucleophilicity.

3.4.4. *Molecular electrostatic potential surface maps (MEPs)*

The molecular electrostatic potential surface (MEP) plays an important role in understanding the electrostatic relationship between molecules [114] and its analysis provides the opportunity to predict the reactivity and possible binding sites. The electrostatic potential is shown with colors; red (most negative electrostatic potential, hydrogen bonding, proton attraction, and reaction with positively charged nuclei) over yellow (weak nucleophilic space) and green (zero potential) to blue (most positive electrostatic potential, electrophilic attack). MEPs of **L1**–**L3** and their related copper(II) complexes (**1**–**3)** are illustrated in Fig. 10. The color codes of these maps (deepest red to deepest blue) are in the ranges of 1.685 to +1.685 eV for **L1**, 1.728 to +1.728 eV for **L2**, 1.982 to +1.982 eV for **L3**, 2.553 to +2.553 eV for **1**, 2.616 to +2.616 eV for **2**, and 2.535 to +2.535 eV for **3**. In MEPs of free ligands **L1**–**L3**, the thioetheric sulfur and imidazolic NH groups are localized in the yellow colored and blue colored regions, respectively. Besides, the benzene rings (light blue and green regions) can be considered as electrophilic sites for nucleophilic attacks [115]. The same phenomena were observed in the coordinated ligands of complexes **1**–**3**. Additionally, the oxygen atoms of sulfate moieties of complexes **1**–**3** are located in the red colored region (most negative electrostatic potential). On the other hand, the electron density on the structure of ligand and complex (dark blue region) with nucleophilic reactivity displays positive density, which is mostly located over NH groups of their imidazole rings. According to these data, amines, benzene rings and oxygen atoms of sulfate groups may be suitable sites to interact with DNA and are responsible for biological activities of **L1**–**L3** and complexes **1**–**3** (*infra vide*).

3.4.5. *Docking simulation data*

In order to get a better understanding of the behavior of the

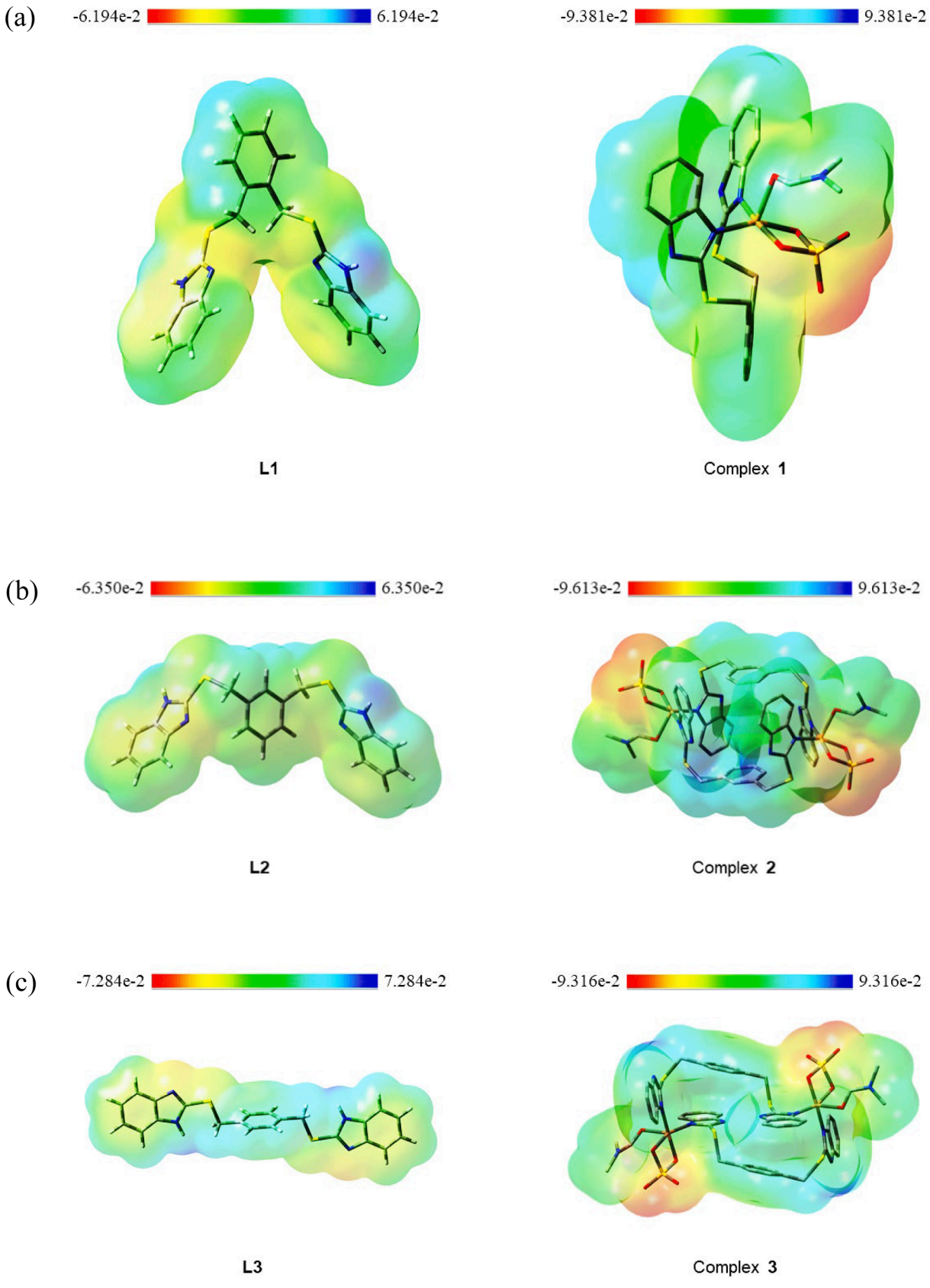

Fig. 10. Molecular electrostatic potential surface map (MEP) of (a) **L1** and complex **1**, (b) **L2** and complex **2**, and (c) **L3** and complex **3** (Hydrogen atoms of all complexes are hidden for clarity).

Table 5
Binding energies in the most negative cluster rank for **L1**–**L3** and complexes **1**–**3** (total runs 300).

Thermodynamic parameters (kcal/mol)	**L1** **run = 83**	**L2** **run = 235**	**L3** **run = 119**	**Complex 1** **run = 284**	**Complex 2** **run = 203**	**Complex 3** **run = 244**
Estimated Free Energy of Binding	9.99	10.26	10.37	8.58	6.68	7.31
Estimated Inhibition Constant, Ki (μM)	0.048	0.030	0.025	0.513	12.66	4.40
Final Intermolecular Energy	11.78	12.05	12.15	9.18	7.87	8.50
vdW + Hbond + desolv Energy	11.75	12.02	12.01	9.04	7.72	8.36
Electrostatic Energy	0.03	0.03	0.15	0.14	0.15	0.14
Final Total Internal Energy	0.68	082	0.63	0.50	1.79	1.34
Torsional Free Energy	1.79	1.79	1.79	0.60	1.19	1.19

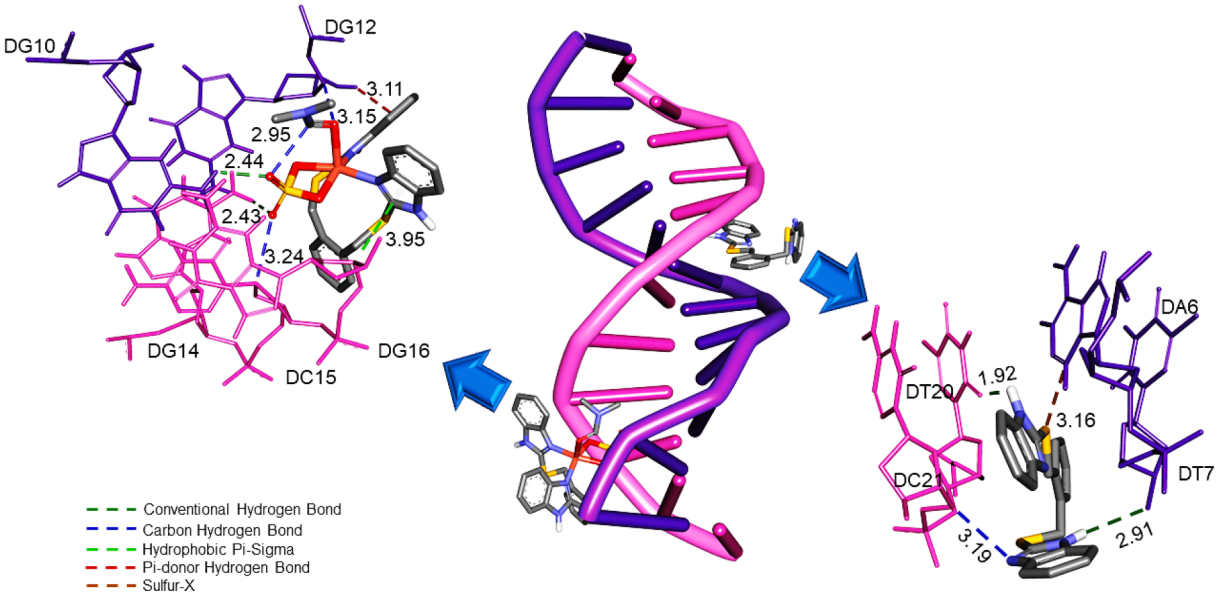

Fig. 11. Representation of docking pose of **L1** and complex **1** interaction with DNA by using Discovery Studio.

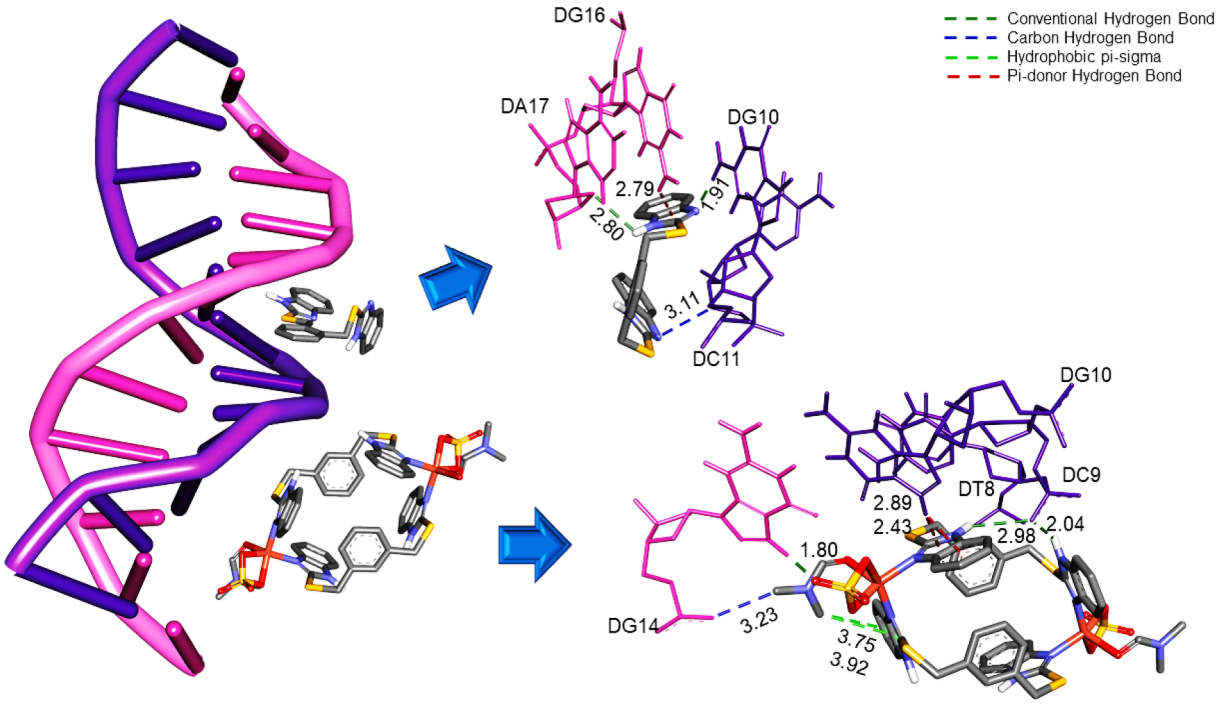

Fig. 12. Representation of docking pose of **L2** and complex **2** interaction with DNA by using Discovery Studio.

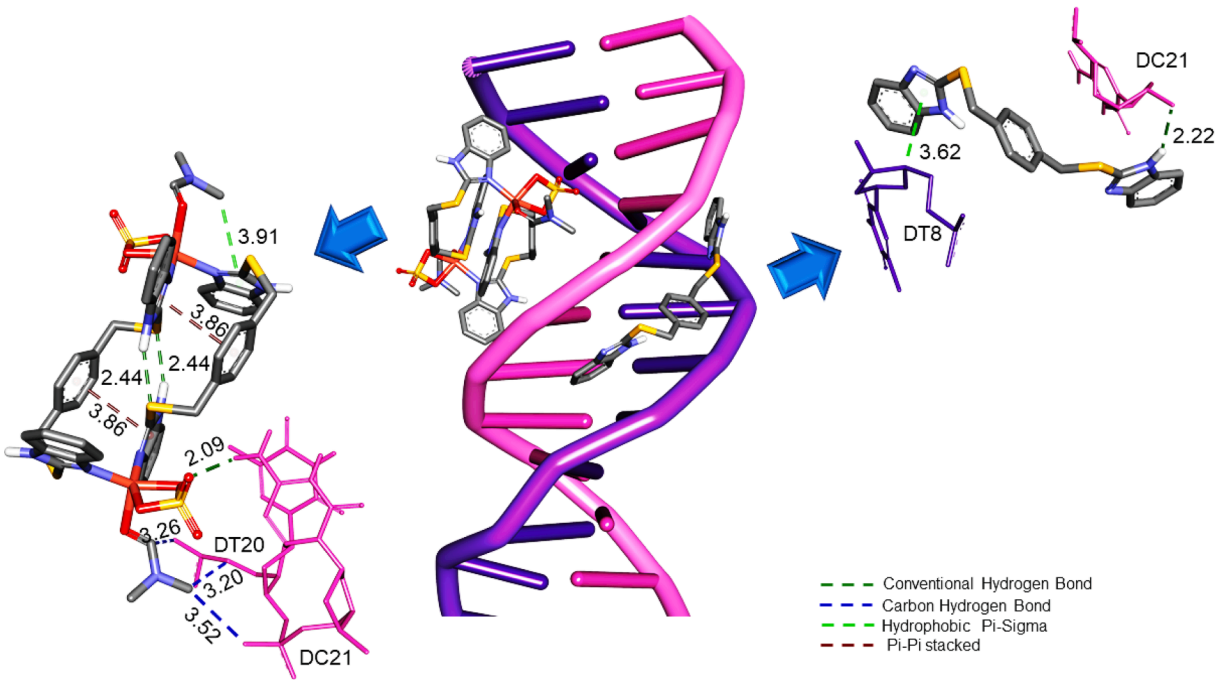

Fig. 13. Representation of docking pose of **L3** and complex **3** interaction with DNA by using Discovery Studio.

synthesized compounds towards DNA, the molecular docking simulation was performed. To show schematically, the interaction of all synthesized compounds with DNA (PDB ID: 1bna) and their binding modes can be followed using the lowest binding energy [77,78]. Thermodynamic parameters for the most negative cluster rank 1 (lowest energy of a 300 runs system) are listed in Table 5, and those of four most negative cluster ranks (1–4) are summarized in Table ST4.

The most negative binding free energies of free ligands in DNA interaction are found to be 9.99 (**L1**), 10.26 (**L2**) and 10.37 (**L3**) kcal/mol for a 300-run system, while those of their related copper(II) complexes **1**, **2** and **3** were found to be 8.58, 6.68 and 7.31 kcal/mol, respectively. These results indicated that **L3** amongst ligands and complex **1** amongst complexes showed a stronger interaction with DNA. Figs. 11–13 illustrate the binding and docking modes of these complexes and their corresponding free ligands to DNA. The docked models revealed that all compounds (except complex **3**) bind in minor grooves of DNA, whereas complex **3** binds to DNA in its major groove.

The docked structures of **L1**–**L3** revealed that the NH group of their benzimidazole rings is involved in strong to weak conventional hydrogen bonds with DNA residues (**L1**: DT20 (1.92 Å) and DT7 (2.91 Å), **L2**: DG10 (1.91 Å) and **L3**: DC21 (2.22 Å)). In addition, the iminic nitrogen atom of benzimidazole moiety in compounds **L1** and **L2** interacts with DNA residue DC21 and DC11, respectively, *via* weak C—H type of H-bonds (3.19 Å for **L1** and 3.11 Å for **L2**). Moreover, compound **L1** shows a weak sulfur-X interaction of 3.16 Å between its thioetheric sulfur atom and nitrogen atom of DA6 residue. While the aromatic benzimidazole ring of compound **L2** exhibits a medium strong hydrophobic hydrogen bond (pi-donor type) of 2.79 Å with DG16 residue, the same ring of compound **L3** interacts with DT8 sequence *via* weak hydrophobic pi-sigma hydrogen bond of 3.62 Å.

On the other hand, the non-coordinated oxygen atoms of sulfate moieties of the docked complexes **1**–**3**, are mainly involved in hydrogen bond interaction with DNA residues. In complex **1**, two such oxygen atoms are coordinated to DG10 and DG14 residues *via* medium strong H-bonds of 2.41 and 2.43 Å, respectively. In this complex, the same oxygen atoms along with the oxygen atom of the dimethylformamide moiety interact with DNA *via* weak intermolecular C—H-bonds (DG12: 3.15 Å and DC15 3.24 Å) and azomethinic CH group of DMF *via* weak intra-complex C—H bond of 2.95 Å. In complexes **2** and **3**, one oxygen atom of their sulfate molecules interacts with the DNA residues through strong to medium H-bonds (**2**: DG14:1.80 Å and **3**: DC21: 2.09 Å).

According to the results of molecular docking studies, only the NH groups of the benzimidazole moieties of complex **2** act as docking sites with DNA residues (DC9: 2.04 and 2.98 Å). This is while, the NH groups in complex **1** are not involved in any interaction and those of complex **3** are involved in medium strong intra-complex interaction through their thioetheric sulfur atoms (2.44 Å). Moreover, the methyl groups of the DMF moiety of **2** and **3** are connected to oxygen atoms of DNA residues *via* weak hydrogen bonds (C—H, **2**: DG14: 3.23 Å and **3**: DT20: 3.26 Å and 3.20 Å and DC21: 3.50 Å). In addition, there are medium to weak pi-donor hydrogen bonds between DNA residues and aromatic benzimidazole rings of complexes **1** (DG12: 3.11 Å) and **2** (DG10: 2.43 and 2.88 Å). These aromatic benzimidazole rings are also responsible for the formation of one weak inter-molecular hydrophobic pi-sigma H-bond of 3.95 Å with DG16 residue in complex **1**, weak intramolecular hydrophobic ones of 3.76 and 3.92 Å in complex **2** and of 3.91 Å in complex **3**. The docked structure of complex **3** exhibited also two intra-complex hydrophobic pi-pi stacked interactions of 3.86 Å between its aromatic benzene and benzimidazole rings.

These data are in sufficient agreement with those of DFT results. All synthesized compounds are located at the groove site of DNA *via* hydrogen bonds, pi-sigma and pi-donor interactions.

4. Conclusions

In this research, three novel copper(II) complexes containing dipodal 2-mercaptobenzimidazole derivatives have been introduced. The molecular structure of binuclear complex **2** revealed that each of the dipodal ligands, **L2**, acts as bridging agent between two metal centers using its endocyclic iminic nitrogen atoms. Each copper(II) ion in complex **2** has distorted square pyramidal geometry.

The antibacterial study revealed that all complexes exhibited higher antibacterial efficacy against the two tested bacterial pathogens (*Escherichia coli ATCC 25922 PTCC 1399* and *Staphylococcus aureus ATCC 6538 PTCC 1112*) compared to their respective ligands. Besides, the screening of all Cu(II) complexes and their related ligands against

human colon cancer cell lines (*HCT-116*) revealed that the cancer cell line viability of all synthesized compounds was dose-dependent. Based on the obtained results, it was observed that complexes **1**–**3** showed greater effectiveness in promoting cancer growth compared with metal-free *bis*-mercaptobenzimidazole derivatives (**L1**–**L3**) and carboplatin. This confirms that metal coordination enhances the activity of the complexes, leading to increased apoptotic induction. In addition, DNA binding studies indicated the interaction between DNA and complexes **1–3** through a dynamic quenching mechanism and hydrophobic forces. In order to support the solid-state structures, the geometric parameters and vibrational frequencies have been investigated using DFT at CAM-B3LYP/6-31G(d) and calcAll-CAM-B3LYP/6-31G(d) level for **L1**–**L3** and **1**–**3**, respectively. The good accordance between the results of experimental and calculated data confirmed the validity of the optimized geometries. Moreover, the decrease in ΔE_{gap} of copper(II) complexes with respect to ligands **L1**–**L3** pointed out the fact that all complexes are chemically more reactive than their corresponding ligands. The MEPs of complexes **1**–**3** revealed that the most negative potential sites are located on non-bonded oxygen atoms of their sulfate moiety, whereas the most positive potential ones are distributed over the hydrogen atoms of NH group of the benzimidazole rings. Furthermore, the optimized structures of the synthesized compounds in DMSO were used for molecular docking simulations. The experimental as well as theoretical results indicated that all complexes interact with DNA in a groove binding mode. According to these results, we believe that this study will be a step forward not only for coordination chemistry in the design and elucidation of copper(II) complexes bearing nitrogen donor ligands but also for bioinorganic and biology research in order to discover new bioactive agents.

CRediT authorship contribution statement

Maryam Kia: Methodology, Investigation. **Mitra Ghassemzadeh:** Writing – review & editing, Writing – original draft, Project administration, Conceptualization. **Mahboube Eslami Moghadam:** Writing – review & editing, Writing – original draft, Investigation. **Maryam Saeidifar:** Methodology, Investigation. **Farshid Mohsenzadeh:** Writing – review & editing. **Olaf Fuhr:** Writing – review & editing, Formal analysis. **Dieter Fenske:** Writing – review & editing, Formal analysis.

Declaration of competing interest

The authors declare that they have no known competing financial interests or personal relationships that could have appeared to influence the work reported in this paper.

Data availability

All data are contained within the article or its supplementary materials as figures or tables.

Acknowledgements

This work was partly carried out with the support of the Karlsruhe Nano Micro Facility (KNMF), a Helmholtz Research Infrastructure at KIT.

References

[1] H. Sung, J. Ferlay, R.L. Siegel, M. Laversanne, I. Soerjomataram, A. Jemal, F. Bray, Global Cancer Statistics 2020: GLOBOCAN estimates of incidence and mortality worldwide for 36 cancers in 185 countries, CA: Cancer J. Clin. 71 (2021) (2020) 209–249, https://doi.org/10.3322/caac.21660.

[2] B. Rosenberg, L. Vancamp, J.E. Trosko, V.H. Mansour, Platinum compounds: a new class of potent antitumour agents, Nature 222 (1969) 385–386, https://doi.org/10.1038/222385a0.

[3] J. Fischer, C.R. Ganellin, Analogue-based Drug Discovery, John Wiley & Sons, 2006, pp. 513, ISBN 9783527607495, Archived from the original on 2016-12-20.

[4] R. Paprocka, M. Wiese-Szadkowska, S. Janciauskiene, T. Kosmalski, M. Kulik, A. Helmin-Basa, Latest developments in metal complexes as anticancer agents, Coord. Chem. Rev. 452 (2022) 214307, https://doi.org/10.1016/j.ccr.2021.214307.

[5] M. Pellei, F. Del Bello, M. Porchia, C. Santini, Zinc coordination complexes as anticancer agents, Coord. Chem. Rev. 445 (2021) 214088, https://doi.org/10.1016/j.ccr.2021.214088.

[6] S. Sen, M. Won, M.S. Levine, Y. Noh, A.C. Sedgwick, J.S. Kim, J.L. Sessler, J. F. Arambula, Metal-based anticancer agents as immunogenic cell death inducers: the past, present, and future, Chem. Soc. Rev. 51 (2022) 1212–1233, https://doi.org/10.1016/j.ccr.2020.213746.

[7] A.C. Santos, L.P. Monteiro, A.C. Gomes, F. Martel, T.M. Santos, B.J.L. Ferreira, NSAID-based coordination compounds for biomedical applications: recent advances and developments, Int. J. Mol. Sci. 23 (2022) 2855, https://doi.org/10.3390/ijms23052855.

[8] N.V. Loginova, H.I. Harbatsevich, N.P. Osipovich, G.A. Ksendzova, T. V. Koval'chuk, G.I. Polozov, Metal complexes as promising agents for biomedical applications, Curr. Med. Chem. 27 (2020) 5213–5249, https://doi.org/10.2174/0929867326666190417143533.

[9] D.M. Cheff, M.D. Hall, A drug of such damned nature. Challenges and opportunities in translational platinum drug research, J. Med. Chem. 60 (2017) 4517–4532, https://doi.org/10.1021/acs.jmedchem.6b01351.

[10] K. Peng, K.B.B. Liang, W. Liu, Z.W. Mao, What blocks more anticancer platinum complexes from experiment to clinic: major problems and potential strategies from drug design perspectives, Coord. Chem. Rev. 449 (2021) 214210, https://doi.org/10.1016/j.ccr.2021.214210 0010-8545.

[11] S. Yarar, I.I. Ozturk, C.N. Banti, N. Panagiotou, C. Papatriantafyllopoulou, M. Manoli, M.J. Manos, A.J. Tasiopoulos, S.K. Hadjikakou, Synthesis, characterization and cytotoxic properties of bismuth (III) chloride complexes with heterocyclic thioamides, Inorg. Chim. Acta 471 (2018) 23–33, https://doi.org/10.1016/j.ica.2017.10.026.

[12] E. Fotopoulou, I. Titilas, L. Ronconi, Metallodrugs as anticancer chemotherapeutics and diagnostic agents: a critical patent review (2010–2020), Recent Pat. Anti-Cancer Drug Discov. 17 (2022) 42–54, https://doi.org/10.2174/1574892816666210907101146.

[13] Q. Peña, A. Wang, O. Zaremba, Y. Shi, H.W. Scheeren, J.M. Metselaar, F. Kiessling, R.M. Pallares, S. Wuttke, T. Lammers, Metallodrugs in cancer nanomedicine, Chem. Soc. Rev. 51 (2022) 2544–2582, https://doi.org/10.1039/D1CS00468A.

[14] S. Parveen, F. Arjmand, S. Tabassum, Development and future prospects of selective organometallic compounds as anticancer drug candidates exhibiting novel modes of action, Eur. J. Med. Chem. 175 (2019) 269–286, https://doi.org/10.1016/j.ejmech.2019.04.062.

[15] M.R. Gill, K.A. Vallis, Transition metal compounds as cancer radiosensitizers, Chem. Soc. Rev. 8 (2019) 540–557, https://doi.org/10.1039/C8CS00641E.

[16] S. Khan, F.A. Alhumaydhi, M.M. Ibrahim, A. Alqahtani, M. Alshamrani, A. S. Alruwaili, A.A. Hassanian, S. Khan, Recent advances and therapeutic journey of Schiff base complexes with selected metals (Pt, Pd, Ag, Au) as potent anticancer agents: a review, Anticancer Agents Med Chem. 22 (2022) 3086–3096, https://doi.org/10.2174/1871520622666220511125600.

[17] W. Liu, R. Gust, Metal N-heterocyclic carbene complexes as potential antitumor metallodrugs, Chem. Soc. Rev. 42 (2013) 755–773, https://doi.org/10.1039/C2CS35314H.

[18] T.S. Prathima, B. Choudhury, M.G. Ahmad, K. Chanda, M.M. Balamurali, Recent developments on other platinum metal complexes as target-specific anticancer therapeutics, Coord. Chem. Rev. 490 (2023) 215231, https://doi.org/10.1016/j.ccr.2023.215231.

[19] C.M. Manzano, D.H. Nakahata, R.E. de Paiva, Revisiting metallodrugs for the treatment of skin cancers, Coord. Chem. Rev. 462 (2022) 214506, https://doi.org/10.1016/j.ccr.2022.214506.

[20] D.M. Yufanyi, H.S. Abbo, S.J. Titinchi, T. Neville, Platinum (II) and Ruthenium (II) complexes in medicine: antimycobacterial and Anti-HIV activities, Coord. Chem. Rev. 414 (2020) 213285, https://doi.org/10.1016/j.ccr.2020.213285.

[21] S.D. Al-Qahtani, A. Alharbi, M.M. Abualnaja, A. Hossan, M. Alhasani, A.M. Abu-Dief, M.E. Khalifa, N.M. El-Metwaly, Synthesis and elucidation of binuclear thiazole-based complexes from Co(II) and Cu(II) ions: conductometry, cytotoxicity and computational implementations for various verifications, J. Mol. Liq. 349 (2022) 118100, https://doi.org/10.1016/j.molliq.2021.118100.

[22] V. Oliveri, Biomedical applications of copper ionophores, Coord. Chem. Rev. 422 (2020) 213474, https://doi.org/10.1016/j.ccr.2020.213474.

[23] S. Zehra, S. Tabassum, F. Arjmand, Biochemical pathways of copper complexes: progress over the past 5 years, Drug Discov. Today 26 (2021) 1086, https://doi.org/10.1016/j.drudis.2021.01.015. N.P.1096.

[24] A.M. Abu-Dief, R.M. El-khatib, S.M. El Sayed, S. Alzahrani, F. Alkhatib, G. El-Sarrag, M. Ismael, Tailoring, structural elucidation, DFT calculation, DNA interaction and pharmaceutical applications of some aryl hydrazone Mn(II), Cu (II) and Fe(III) complexes, J. Mol. Struct. 1244 (2021) 131017, https://doi.org/10.1016/j.molstruc.2021.131017.

[25] A. Kellett, Z. Molphy, C. Slator, V. McKee, N.P. Farrell, Molecular methods for assessment of non-covalent metallodrug–DNA interactions, Chem. Soc. Rev. 48 (2019) 971–988, https://doi.org/10.1039/c8cs00157j.
[26] R. Olar, M. Badea, M. Bacalum, M. Răileanu, L.L. Ruţă, I.C. Farcaşanu, A. M. Rostas, I.D. Vlaicu, M. Popa, M.C. Chifiriuc, Antiproliferative and antibacterial properties of biocompatible copper(II) complexes bearing chelating N, N- heterocycle ligands and potential mechanisms of action, Biometals 34 (2021) 1155–1172, https://doi.org/10.1007/s10534-021-00334-9.
[27] C. Molinaro, A. Martoriati, L. Pelinski, K. Cailliau, Copper complexes as anticancer agents targeting topoisomerases I and II, Cancers 12 (2020) 2863, https://doi.org/10.3390/cancers12102863.
[28] Y. Jiang, Z. Huo, X. Qi, T. Zuo, Z. Wu, Copper-induced tumor cell death mechanisms and antitumor theragnostic applications of copper complexes, Nanomedicine 17 (2022) 303–324, https://doi.org/10.2217/nnm-2021-0374.
[29] C. Abate, F. Carnamucio, O. Giuffrè, C. Foti, Metal-based compounds in antiviral therapy, Biomolecules 12 (2022) 933, https://doi.org/10.3390/biom12070933.
[30] J. Gopal, M. Muthu, I. Sivanesan, A comprehensive survey on the expediated anti-COVID-19 options enabled by metal complexes—tasks and trials, Molecules 28 (2023) 3354, https://doi.org/10.3390/molecules28083354.
[31] R.E. de Paiva, A.M. Neto, I.A. Santos, A.C. Jardim, P.P. Corbi, F.R. Bergamini, What is holding back the development of antiviral metallodrugs? A literature overview and implications for SARS-CoV-2 therapeutics and future viral outbreaks, Dalton Trans. 49 (2020) 16004–16033, https://doi.org/10.1039/D0DT02478C.
[32] G. Psomas, Copper (II) and zinc (II) coordination compounds of non-steroidal anti-inflammatory drugs: structural features and antioxidant activity, Coord. Chem. Rev. 412 (2020) 213259, https://doi.org/10.1016/j.ccr.2020.213259.
[33] Q.U.A. Sandhu, M. Pervaiz, A. Majid, U. Younas, Z. Saeed, A. Ashraf, R.R. M. Khan, S. Ullah, F. Ali, S. Jelani, Schiff base metal complexes as anti-inflammatory agents, J. Coord. Chem. 76 (2023) 1094–1118, https://doi.org/10.1080/00958972.2023.2226794.
[34] A. Frei, A.D. Verderosa, A.G. Elliott, J. Zuegg, M.A. Blaskovich, Metals to combat antimicrobial resistance, Nat. Rev. Chem. 7 (2023) 202–224, https://doi.org/10.1038/s41570-023-00463-4.
[35] H. O'Brien, T. Davoodian, M.D. Johnson, The promise of copper ionophores as antimicrobials, Curr. Opin. Microbiol. 7 (2023) 102355, https://doi.org/10.1016/j.mib.2023.102355.
[36] M. Fanelli, M. Formica, V. Fusi, L. Giorgi, M. Micheloni, P. Paoli, New trends in platinum and palladium complexes as antineoplastic agents, Coord. Chem. Rev. 310 (2016) 41–79, https://doi.org/10.1016/j.ccr.2015.11.004.
[37] C.B. Scarim, R.L. de Farias, A.V. de Godoy Netto, C.M. Chin, J.L. Dos Santos, F. R. Pavan, Recent advances in drug discovery against Mycobacterium tuberculosis: metal-based complexes, Eur. J. Med. Chem. 214 (2021) 113166, https://doi.org/10.1016/j.ejmech.2021.113166.
[38] P. Sudhindra, S.A. Sharma, N. Roy, P. Moharana, P. Paira, Recent advances in cytotoxicity, cellular uptake and mechanism of action of ruthenium metallodrugs: a review, Polyhedron 192 (2020) 114827, https://doi.org/10.1016/j.poly.2020.114827.
[39] G.L. Parrilha, R.G. dos Santos, H. Beraldo, Applications of radiocomplexes with thiosemicarbazones and bis(thiosemicarbazones) in diagnostic and therapeutic nuclear medicine, Coord. Chem. Rev. 458 (2022) 214418, https://doi.org/10.1016/j.ccr.2022.214418.
[40] E. Yousif, A. Majeed, K. Al-Sammarrae, N. Salih, J. Salimon, B. Abdullah, Metal complexes of Schiff base: preparation, characterization and antibacterial activity, Arab. J. Chem. 10 (2017) S1639–S1644, https://doi.org/10.1016/j.arabjc.2013.06.006.
[41] C. Elamathi, F.R. Fronczek, A. Madankumar, R. Prabhakaran, Synthesis and spectral characterizations of water-soluble Cu(II) complexes containing N-heterocyclic chelates: cell-proliferation, antioxidant and nucleic acid/serum albumin interactions, New J. Chem. 44 (2020) 4158–4170, https://doi.org/10.1039/C9NJ04136B.
[42] D.K. Kozlica, A. Kokalj, I. Milošev, Synergistic effect of 2-mercaptobenzimidazole and octylphosphonic acid as corrosion inhibitors for copper and aluminium–An electrochemical, XPS, FTIR and DFT study, Corros. Sci. 182 (2021) 109082, https://doi.org/10.1016/j.corsci.2020.109082.
[43] H. Lgaz, S. Masroor, M. Chafiq, M. Damej, A. Brahmia, R. Salghi, M. Benmessaoud, I.H. Ali, M.M. Alghamdi, A. Chaouiki, I.M. Chung, Evaluation of 2-mercaptobenzimidazole derivatives as corrosion inhibitors for mild steel in hydrochloric acid, Metals 10 (2020) 357, https://doi.org/10.3390/met10030357.
[44] W. Zhao, J. He, P. Yu, X. Jiang, L. Zhang, Recent progress in the rubber antioxidants: a review, Polym. Degrad. Stab. 207 (2022) 110223, https://doi.org/10.1016/j.polymdegradstab.2022.110223.
[45] S. Rulhania, S. Kumar, B. Nehra, G.D. Gupta, V. Monga, An insight into the medicinal perspective of synthetic analogs of imidazole, J. Mol. Struct. 1232 (2021) 129982, https://doi.org/10.1016/j.molstruc.2021.129982.
[46] M. Nardi, N.C.H. Cano, S. Simeonov, R. Bence, A. Kurutos, R. Scarpelli, D. Wunderlin, A.A. Procopio, Review on the green synthesis of benzimidazole derivatives and their pharmacological activities, Catalysts 13 (2023) 392, https://doi.org/10.3390/catal13020392.
[47] H.E. Hashem, Y. El Bakri, An overview on novel synthetic approaches and medicinal applications of benzimidazole compounds, Arab. J. Chem. 14 (2021) 103418, https://doi.org/10.1016/j.arabjc.2021.103418.
[48] M.V. De Almeida, M.V.N. De Souza, S.H. Cardoso, J.V. De Assis, Synthesis of 2-mercaptobenzothiazole and 2-mercaptobenzimidazole derivatives condensed with carbohydrates as a potential antimicrobial agent, J. Sulfur Chem. 28 (2007) 17–22, https://doi.org/10.1080/17415990601055291.
[49] M.T. Khan, H. Nadeem, A.U. Khan, M. Abbas, M. Arif, N.S. Malik, Z. Malik, I. Javed, Amino acid conjugates of 2-mercaptobenzimidazole provide better anti-inflammatory pharmacology and improved toxicity profile, Drug Dev. Res. 81 (2020) 1057–1072, https://doi.org/10.1002/ddr.21728.
[50] S.R. Brishty, M.J. Hossain, M.U. Khandaker, M.R.I. Faruque, H. Osman, S. M. Rahman, A comprehensive account on recent progress in pharmacological activities of benzimidazole derivatives, Front. Pharmacol. 12 (2021) 762807, https://doi.org/10.3389/fphar.2021.762807.
[51] Y.H. Chen, Three new luminescent Cd(II) coordination polymers constructed from 2-mercaptobenzimidazole and different auxiliary ligands, Inorg. Nano-Met. Chem. (2021) 1–7, https://doi.org/10.1080/24701556.2021.2014525.
[52] P. Sun, M. Xie, L.M. Zhang, J.X. Liu, J. Wu, D.S. Li, S.F. Yuan, T. Wu, D. Li, Ultrastable anti-acid "Shield" in layered silver coordination polymers, Angew. Chem. Int. Ed. 61 (2022) e202209971, https://doi.org/10.1002/anie.202209971.
[53] P. Chooto, S. Saithong, W. Aemaeg, S. Vataporn, C. Pakawatchai, C. Innuphat, S. Duangthong, W. Puetpaiboon, Syntheses, crystal structures and Hirshfeld surface analyses of bis (2-mercaptobenzimidazole) bromo-and iodocopper(I) complexes, Acta Crystallogr. E 78 (2022) 519–524, https://doi.org/10.1107/S2056989022004224 5.
[54] I.I. Ozturk, S. Yarar, M. Gürgan, D. Ceyhan, N. Panagiotou, A.J. Tasiopoulos, S. Demirkesen, C. Aral, Novel binuclear antimony(III) halide complexes of 5-methoxy-2-mercaptobenzimidazole: synthesis, structural characterization, and biological studies, J. Coord. Chem. 73 (2020) 485–505, https://doi.org/10.1080/00958972.2020.1735003.
[55] R. Balamurugan, M. Palaniandavar, R.S. Gopalan, Trigonal planar copper (I) complex: synthesis, structure, and spectra of a redox pair of novel copper(II/I) complexes of tridentate bis(benzimidazol-2′-yl) ligand framework as models for electron-transfer copper proteins, Inorg. Chem. 40 (2001) 2246–2255, https://doi.org/10.1021/ic0003372.
[56] P.J. Birker, J. Helder, G. Henkel, B. Krebs, J. Reedijk, Synthesis and spectroscopic characterization of copper(I) and copper(II) complexes with 1,6-bis(2-benzimidazolyl)-2,5-dithiahexane (BBDH). X-ray structure of trigonal-bipyramidal coordinated [Cu(BBDH)Cl]Cl•$2C_2H_5OH$, Inorg. Chem. 21 (1982) 357–363, https://doi.org/10.1021/ic00131a064.
[57] A.W. Addison, T.N. Rao, J. Reedijk, J. van Rijn, G.C. Verschoor, Synthesis, structure, and spectroscopic properties of copper (II) compounds containing nitrogen–sulphur donor ligands; the crystal and molecular structure of aqua[1,7-bis(N-methylbenzimidazol-2′-yl)-2,6-dithiaheptane]copper(II) perchlorate, J. Chem. Soc. Dalton Trans. (1984) 1349–1356, https://doi.org/10.1039/DT9840001349.
[58] M. Imran, A. Mix, B. Neumann, H.G. Stammler, U. Monkowius, P. Gründlinger, N. W. Mitzel, Hemi-and holo-directed lead(II) complexes in a soft ligand environment, Dalton Trans. 44 (2015) 924–937, https://doi.org/10.1039/C4DT01406E.
[59] J.K. Cheng, X. Zhang, M.J. Zhang, Y.G. Yao, An exceptionally stable Pb (II) arene compound, Inorg. Chem. Commun. 17 (2012) 88–90, https://doi.org/10.1016/j.inoche.2011.12.021.
[60] S. Amiri, M. Ghassemzadeh, B. Neumüller, F. Mohsenzadeh, A new silver(I) coordination polymer containing bitopic 1,2,4-triazole derivative: synthesis, structural investigation, and thermal behavior, Polyhedron 197 (2021) 115039, https://doi.org/10.1016/j.poly.2021.115039 0277-5387.
[61] S. Bahemmat, M. Ghassemzadeh, M. Afsharpour, K. Harms, Synthesis, characterization and crystal structure of a Pd(II) complex containing a new bis-1,2,4-triazole ligand: a new precursor for the preparation of Pd(0) nanoparticles, Polyhedron 89 (2015) 196–202, https://doi.org/10.1016/j.poly.2014.12.050.
[62] L. Heidari, M. Ghassemzadeh, D. Fenske, O. Fuhr, M. Saeidifar, F. Mohsenzadeh, Unprecedented palladium(II) complex containing dipodal 1,3,4-thiadiazole derivatives: synthesis, structure, and biological and thermal investigations, New J. Chem. 44 (2020) 16769–16775, https://doi.org/10.1039/d0nj02918a.
[63] S. Bahemmat, M. Ghassemzadeh, B. Neumüller, A new silver(I) coordination polymer containing 3-methylthio-(1H)-1,2,4-triazole as precursor for preparation of silver nanorods, Inorg. Chim. Acta 453 (2015) 159–166, https://doi.org/10.1016/j.ica.2015.06.016.
[64] L. Heidari, M. Ghassemzadeh, D. Fenske, O. Fuhr, F. Mohsenzadeh, V. Bon, 3D coordination polymers constructed from d^{10} metal ions, flexible 1,2,4-triazole derivatives and aromatic tetracarboxylates: syntheses, structures, thermal and luminescent properties, J. Solid State Chem. 296 (2021) 122011, https://doi.org/10.1016/j.jssc.2021.122011.
[65] A. Gouranourimi, M. Ghassemzadeh, S. Bahemmat, B. Neumüller, R. Tonner, New palladium(II) complexes containing 3-mercapto-1,2,4-triazole ligands: synthesis, characterization, crystal structure, and density functional theory calculations, Monatsh. Chem. 146 (2015) 57–67, https://doi.org/10.1007/s00706-014-1280-z.
[66] A. Husain, C.S. Devi, B. Anupama, Synthesis, characterization, DNA binding, antioxidant and microbial activity of tetrazole ring based complexes, J. Mol. Struct. 1291 (2023) 135963, https://doi.org/10.1016/j.molstruc.2023.135963.
[67] A. Mamindla, M. Varadhan, R. Kartikeyan, A. Amuthamozhi, M.A. Akbarsha, V. Rajendiran, Comparative DNA-/BSA-binding, DNA cleavage, and cytotoxic properties of copper (II) amino/salicyl-phenolate Schiff bases (phen) complexes that induce generation of phenoxyl radicals, Polyhedron 243 (2023) 116534, https://doi.org/10.1016/j.poly.2023.116534.

[68] K. Aoki, K. Aikawa, 2-mercaptobenzimidazole derivatives and antihyperlipemic agent or antiarteriosclerotic agent containing the same, U.S. Patent 5962493, 1999.
[69] O.V. Dolomanov, L.J. Bourhis, R.J. Gildea, J.A.K. Howard, H. Puschmann, OLEX2: a complete structure solution, refinement, J. Appl. Cryst. 42 (2009) 339–341, https://doi.org/10.1107/S0021889808042726.
[70] G.M. Sheldrick, SHELXT-Integrated Space-Group and Crystal-Structure Determination, Acta Cryst. A 71 (2015) 3–8, https://doi.org/10.1107/S2053273314026370.
[71] G.M. Sheldrick, Crystal structure refinement with SHELXL, Acta Cryst. C 71 (2015) 3–8, https://doi.org/10.1107/S2053229614024218.
[72] M. Murali, J. Latha, P.A. Prakash, S. Sangeetha, B. Selvakumaran, M.S.M. Jaabir, Characterization of $[Ru(bpy)_2(diamine)]^{2+}$ complexes and their DNA binding and cleavage, BSA interaction, cytotoxic, and anticancer mechanistic properties, Polyhedron 223 (2022) 115925, https://doi.org/10.1016/j.poly.2022.115925.
[73] A.H. Bashal, K.D. Khalil, A.M. Abu-Dief, M.A. El-Atawy, Cobalt oxide-chitosan based nanocomposites: synthesis, characterization and their potential pharmaceutical applications, Int. J. Biol. Macromol. 253 (2023) 126856, https://doi.org/10.1016/j.ijbiomac.2023.126856.
[74] Z.F. Zeng, Q.P. Huang, J.H. Cai, G.J. Zheng, L.J. Qin, Q.C. Huang, Y.H. Wei, CT-DNA/HSA binding interactions and cytotoxicity activity of a new copper(II) complex, Inorg. Chem. Commun. 133 (2021) 108917, https://doi.org/10.1016/j.inoche.2021.108917.
[75] N.E. Alshaikh, M. Zaki, A.A. Sharfalddin, N.S. Al-Radadi, M.A. Hussien, W. M. Hassan, Synthesis, structural characterization, DNA/HSA binding, molecular docking and anticancer studies of some D-Luciferin complexes, Arab. J. Chem. 16 (2023) 104845, https://doi.org/10.1016/j.arabjc.2023.104845.
[76] M. Feizi-Dehnayebi, E. Dehghanian, H. Mansouri-Torshizi, DNA/BSA binding affinity studies of new Pd (II) complex with SS and NN donor mixed ligands via experimental insight and molecular simulation: preliminary antitumor activity, lipophilicity, and DFT perspective, J. of Mol. Liq. 344 (2021) 117853, https://doi. org/10.1016/j.molliq.2021.117853.
[77] A. Jafari, M. Eslami Moghadam, H. Mansouri-Torshizi, Green synthesis and bioactivity of aliphatic N-substituted glycine derivatives, ACS Omega 8 (2023) 30158–30176, https://doi.org/10.1021/acsomega.3c02828.
[78] M. Eslami Moghadam, M. Rezaeisadat, E. Shahryari, H. Mansouri-Torshizi, M. Heydari, Biological interaction of Pt complex with imidazole derivative as an anticancer compound with DNA: experimental and theoretical studies, Int. J. Biol. Macromol. 249 (2023) 126097, https://doi.org/10.1016/j.ijbiomac.2023.126097.
[79] G.W.T.M.J. Frisch, H.B. Schlegel, G.E. Scuseria, M.A. Robb, J.R. Cheeseman, G. Scalmani, V. Barone, B. Mennucci G.A. Petersson, H. Nakatsuji, M. Caricato, X. Li, H.P. Hratchian, A.F. Izmaylov, J. Bloino, G. Zheng, J.L. Sonnenberg, M. Hada, M. Ehara, K. Toyota, R. Fukuda, J. Hasegawa, M. Ishida, T. Nakajima, Y. Honda, O. Kitao, H. Nakai, T. Vreven, J.A. Montgomery Jr., J.E. Peralta, F. Ogliaro, M. Bearpark, J.J. Heyd, E. Brothers, K.N. Kudin, V.N. Staroverov, R. Kobayashi, J. Normand, K. Raghavachari, A. Rendell, J.C. Burant, S.S. Iyengar, J. Tomasi, M. Cossi, N. Rega, J.M. Millam, M. Klene, J.E. Knox, J.B. Cross, V. Bakken, C. Adamo, J. Jaramillo, R. Gomperts, O.Y. Stratmann, A.J. Austin, R. Cammi, C. Pomelli, J. W. Ochterski, R.L. Martin, K. Morokuma, V.G. Zakrzewski, G.A. Voth, P. Salvador, J.J. Dannenberg, S. Dapprich, A.D. Daniels, D. Farkas, J.B. Foresman, J.V. Ortiz, J. Cioslowski, D.J. Fox Gaussian 09; Gaussian, Inc.: Wallingford, CT, USA (2009).
[80] T. Yanai, D.P. Tew, N.C. Handy, A new hybrid exchange–correlation functional using the Coulomb-attenuating method (CAM-B3LYP), Chem. Phys. Lett. 393 (2004) 51–57, https://doi.org/10.1016/j.cplett.2004.06.011.
[81] M. Eslami Moghadam, M. Rezaeisadat, H. Mansouri-Torshizi, S. Hosseinzadeh, H. Daneshyar, New anticancer potential Pt complex with tertamyl dithiocarbamate ligand: synthesis, DNA targeting behavior, molecular dynamic, and biological activity, J. Mol. Liq. 379 (2023) 121651, https://doi.org/10.1016/j.molliq.2023.121651.
[82] M. Ahmad, K.A. Siddiqui, Cu(II)-based coordination polymer encapsulated formate: unveiling efficient photocatalytic degradation of Rose Bengal dye and remarkable sensing of DMF, acetone and acetonitrile, J. Mol. Struct. 1280 (2023) 135055, https://doi.org/10.1016/j.molstruc.2023.135055.
[83] H.A. El-Boraey, A.A.S. El-Din, Gamma ray irradiated binuclear and mononuclear transition metal complexes with polydentate ligand: template synthesis, spectral, XRD, morphology, solid electrical conductivity and antimicrobial activity, J. Mol. Struct. 1281 (2023) 134842, https://doi.org/10.1016/j.molstruc.2022.134842.
[84] A.A. Ajibola, F. Perveen, K. Jan, I.I. Anibijuwon, S.E. Shaibu, L. Sieroń, W. A. Maniukiewicz, Five-coordinate copper(II) complex constructed from sterically hindered 4-chlorobenzoate and benzimidazole: synthesis, crystal structure, hirshfeld surface analysis, DFT, docking studies and antibacterial activity, Crystals 10 (2020) 991, https://doi.org/10.3390/cryst10110991.
[85] C.C. Gatto, E.D.A. Duarte, G.S. Liarte, T.S. Silva, M.B. Santiago, C.H. Martins, Transition metal complexes with 2-acetylpyridine-ethylcarbazate: noncovalent interactions in their structures and antimicrobial studies, J. Coord. Chem. 73 (2020) 1573–1590, https://doi.org/10.1080/00958972.2020.1777408.
[86] A.B.P. Lever, Inorganic Electronic Spectroscopy, Elsevier, Amsterdam, 1984, p. 553.
[87] H.M. Abd El-Lateef, A.D.M. Mohamad, M.R. Shehata, A.M. Abu-Dief, Targeted synthesis of two iron(III) tetradentate dibasic chelating Schiff base complexes toward inhibition of acidic induced steel corrosion: empirical and DFT insights, Appl. Organomet. Chem. 36 (2022) e6718.
[88] J.Q. Chen, J. Guo, Z.B. Dong, Three-component synthesis of 2-alkylthiobenzoazoles in aqueous media, Synthesis 52 (2020) 1927–1933, https://doi.org/10.1055/s-0039-1690854.
[89] M. Kubicki, G. Dutkiewicz, J.P. Jasinski, R.J. Butcher, M.S. Siddegowda, H. S. Yathirajan, B. Narayana, Ordering of the water molecule in the crystal structure of 2-[3-methyl-4-(2,2,2-trifluoroethoxy)-2-pyridinyl]methylthio-1H-benzimidazole hydrate (lanso-prazole sulphide hydrate), J. Chem. Crystallog. 42 (2012) 245–250, https://doi.org/10.1007/s10870-011-0232-2.
[90] X. Liu, Z.B. Dong, Chemoselective Chan-Lam coupling reactions between benzimidazoline-2-thiones and arylboronic acids, J. Org. Chem. 84 (2019) 11524–11532, https://doi.org/10.1021/acs.joc.9b01370.
[91] L. Zheng, W. Mei, X. Zou, Y. Zhong, Y. Wu, L. Deng, Y. Wang, B. Yang, W. Guo, DBU-promoted deaminative thiolation of 1H-benzo[d]imidazol-2-amines and benzo[d]oxazol-2-amines, J. Org. Chem. 88 (2023) 272–284, https://doi.org/10.1021/acs.joc.2c02297.
[92] M. Saylam, F.A. Köse, A. Pabuccuoglu, D.B. Celepci, M. Aygün, V. Pabuccuoglu, Design, synthesis, and biological activity studies on benzimidazole derivatives targeting myeloperoxidase, Eur. J. Med. Chem. 248 (2023) 115083, https://doi.org/10.1016/j.ejmech.2022.115083.
[93] C.J. Matthews, W. Clegg, M.R.J. Elsegood, T.A. Leese, D. Thorp, P. Thornton, J. C. Lockhart, Synthesis and crystal structures of some bis-benzimidazoles,-benzothiazoles and-benzoxazoles by an alternative route: their complexation with copper(II) salts, J. Chem. Soc., Dalton Trans. 8 (1996) 1531–1538, https://doi.org/10.1039/DT9960001531.
[94] M. Gupta, S.K. Das, P. Mathur, A.W. Cordes, Synthesis, crystal structure and spectral studies of Cu (II)/Cu(I) complexes derived from diamide bisbenzimidazole ligand, Inorg. Chim. Acta 353 (2003) 197–205, https://doi.org/10.1016/S0020-1693(03)00308-6.
[95] B.G. Cassemiro, J.S. Santos, W.X. Oliveira, E.C. Pereira-Maia, B.R. Galvao, W. D. do Pim, P.P. Silva-Caldeira, Dinuclear copper(II) complex with a benzimidazole derivative: crystal structure, theoretical calculations, and cytotoxic activity, Appl. Organomet. Chem. 34 (2020) e5425, https://doi.org/10.1002/aoc.5425.
[96] Y. Qiu, Y. Miao, Z. Wang, Z. Li, Z. OuYang, L. Yang, W. Lin, W. Feng, W. Dong, Syntheses, structures, electrochemical and optical properties of four transition metal complexes based on the 1-triazolyl-3-benzimidazolyltriazene ligand, RSC Adv. 6 (2016) 4969–4978, https://doi.org/10.1039/C5RA21057G.
[97] A.X. Tian, X.B. Ji, N. Sun, R. Xiao, Y.Y. Zhao, H.P. Ni, Y. Tian, J. Ying, Four new coordination polymers constructed by 2-(4-Thiazolyl)benzimidazole and 1,3,5-benzenetricarboxylic acid, J. Chem. Crystallogr. 47 (2017) 1–9, https://doi.org/10.1007/s10870-016-0674-7.
[98] S. Thatituri, B. Govindugari, V.R.R. Chittireddy, Carboxylate-bridged Cu(II) coordination polymeric complex: synthesis, crystal structure, magnetic properties, DNA binding and electrochemical studies, J. Chem. Sci. 129 (2017) 1171–1181, https://doi.org/10.1007/s12039-017-1330-2.
[99] P. Masárová, V. Kuchtanin, M. Mazúr, J. Moncol, Crystal structures and spectroscopic properties of copper(II)–dipicolinate complexes with benzimidazole ligands, Transit. Met. Chem. 43 (2018) 507–516, https://doi.org/10.1007/s11243-018-0236-2.
[100] S.U. Khan, M. Akhtar, F.U. Khan, J. Peng, A. Hussain, H. Shi, J. Du, G. Yan, Y. Li, Polyoxometalates decorated with metal-organic moieties as new molecular photo- and electro-catalysts, J. Coord. Chem. 71 (2018) 2604–2621, https://doi.org/10.1080/00958972.2018.1500694.
[101] S.E. Korolenko, E.A. Malinina, V.V. Avdeeva, A.S. Kubasov, L.V. Goeva, E. A. Ugolkova, V.V. Minin, A.S. Burlov, L.N. Divaeva, N.T. Kuznetsov, Chemical stability of 1-substituted 2-aldimine- and 2-azobenzimidazoles under copper-promoted autoxidation, Inorg. Chim. Acta 539 (2020) 121038, https://doi.org/10.1016/j.ica.2022.121038.
[102] B. Greener, S.P. Foxon, P.H. Walton, Syntheses and structures of a range of metal complexes with the ligand cis, cis-1,3,5-(E, E)-tris(phenylpropenylideneamino) cyclohexane, New J. Chem. 24 (2000) 269–273, https://doi.org/10.1039/b000441n.
[103] R. Cejudo, G. Alzuet, J. Borrás, M. Liu-González, F. Sanz-Ruiz, Crystal structure, magnetic and spectroscopic properties of copper(II) formato dimethylformamide: a new tetracarboxylato-bridged copper(II) dimer, Polyhedron 21 (2002) 1057–1061, https://doi.org/10.1016/s0277-5387(02)00935-x.
[104] P. Drożdżewski, A. Brożyna, M. Kubiak, New binuclear copper(II) complex with 2-thiopheneacetic acid. Synthesis, X-ray diffraction and vibrational studies of bis(N, N-dimethylformamide)tetra(2-thiopheneacetato) dicopper(II), J. Mol. Struct. 707 (2004) 131–137, https://doi.org/10.1016/j.molstruc.2004.06.034.
[105] J. Baharara, N. Hosseini, T.R. Farzin, Extremely low frequency electromagnetic field sensitizes cisplatin-resistant human ovarian adenocarcinoma cells via P53 activation, Cytotechnology 68 (2016) 1403–1413, https://doi.org/10.1007/s10616-015-9900-y.
[106] J. Hu, S. Chen, R. Mao, C. Liao, H. Yang, Cytotoxicity, dual-targeting apoptosis induction evaluation of multinuclear cu complexes based on pyrazine-benzimidazole derivative, J. Inorg. Biochem. 186 (2018) 246–256, https://doi.org/10.1016/j.jinorgbio.2018.06.014.
[107] J.A. Zhao, S. Zhi, H. Yu, J. Zhang, J. Zhang, J. Hu, Synthesis, crystal structure, DNA/BSA interaction and in vitro antitumor activity of N-heterocycle Cu (II) and Co (II) complexes, J. Coord. Chem. 70 (2017) 3110–3131, https://doi.org/10.1080/00958972.2017.1372573.
[108] N. Fattahian Kalhor, M. Saeidifar, H. Ramshini, A.A. Saboury, Interaction, cytotoxicity and sustained release assessment of a novel anti-tumor agent using bovine serum albumin nanocarrier, J. Biomol. Struct. Dyn. 38 (2020) 2546–2558, https://doi.org/10.1080/07391102.2019.1638303.
[109] A. Georgieva, G. Popov, A. Shkondrov, R. Toshkova, I. Krasteva, M. Kondeva-Burdina, V. Manov, Antiproliferative and Antitumour activity of saponins from

Astragalus glycyphyllos on myeloid Graffi tumour, J. Ethnopharmacol. 267 (2020) 113519, https://doi.org/10.1016/j.jep.2020.113519.
[110] C.G. Li, Y.M. Chai, L.Q. Chai, L.Y. Xu, Novel zinc(II) and nickel(II) complexes of a quinazoline-based ligand with an imidazole ring: synthesis, spectroscopic property, antibacterial activities, time-dependent density functional theory calculations and Hirshfeld surface analysis, Appl. Organomet. Chem. 36 (2022) e6622, https://doi.org/10.1002/aoc.6622.
[111] I.M. Alecu, J. Zheng, Y. Zhao, D.G. Truhlar, Computational thermochemistry: scale factor databases and scale factors for vibrational frequencies obtained from electronic model chemistries, J. Chem. Theory Comput. 6 (2010) 2872–2887, https://doi.org/10.1021/ct100326h.
[112] Y. El Bakri, S.K. Mohamed, A. Ahsin, E.A. Bakhite, I.S. Marae, S.A.H. Al-waleedy, J.T. Mague, R. Al-Salahi, X-ray diffraction, spectroscopy, optical properties, NPA, NBO, FMO, and hirshfeld surface analyses of two newly synthesized piperidinium ionic liquids, Crystals 13 (2023) 1583, https://doi.org/10.3390/cryst13111583.
[113] R. Godwini, J.C. Monicka, S.G. Victoria, Analyses on the reactivity, topology and bioactivity of Fluazinam using density functional theory, Chem. Phys. Impact 7 (2023) 100309, https://doi.org/10.1016/j.chphi.2023.100309.
[114] L. Liu, L. Miao, L. Li, F. Li, Y. Lu, Z. Shang, J. Chen, Molecular electrostatic potential: a new tool to predict the lithiation process of organic battery materials, J. Phys. Chem. Lett. 9 (2018) 3573–3579, https://doi.org/10.1021/acs.jpclett.8b01123.
[115] Z. Hosseini-Hashemi, M. Mirzaei, M. Eslami Moghadam, Property evaluation of two anticancer candidate platinum complexes with N-isobutyl glycine ligand against human colon cancer, Biometals 35 (2022) 987–1009, https://doi.org/10.1007/s10534-022-00418-0.